arXiv:1401.0848v1 [cond-mat.mes-hall] 4 Jan 2014

Experimental Discovery of Topological Surface States - A New Type of 2D Electron Systems

M. Zahid Hasan,[1,2] Su-Yang Xu,[1,3] David Hsieh,[1,4] L. Andrew Wray,[1,3] and Yuqi Xia[1]

[1] *Joseph Henry Laboratories, Department of Physics, Princeton University, Princeton, NJ 08544, USA*
[2] *Princeton Institute for the Science and Technology of Materials, School of Engineering and Applied Science, Princeton University, Princeton NJ 08544, USA*
[3] *Advanced Light Source, Lawrence Berkeley National Laboratory, Berkeley, California 94305, USA*
[4] *Department of Physics, California Institute of Technology, Pasadena, CA 91125, USA*

Topological Surface States (TSS) represent new types of two dimensional electron systems with novel and unprecedented properties distinct from any quantum Hall-like or spin-Hall effects. Their Z_2 topological order can be realized at room temperatures without magnetic fields and they can be turned into magnets, exotic superconductors or Kondo insulators leading to worldwide interest and activity in the topic. We review the basic concepts defining such topological matter and the experimental discovery via the key experimental probe (spin-ARPES) that revealed the Z_2 topological order in the bulk of these spin-orbit interaction dominated insulators for the first time. This review focuses on the key results that demonstrated the fundamental Z_2 topological properties such as spin-momentum locking, non-trivial Berrys phases, mirror Chern number, absence of backscattering, bulk-boundary correspondence (topology), protection by time-reversal and other discrete (mirror) symmetries and their remarkable persistence up to the room temperature elaborating on results first briefly discussed in an early review by M.Z. Hasan and C.L. Kane [Rev. of Mod. Phys., 82, 3045 (2010)]. Additionally, key results on broken symmetry phases such as quantum magnetism and superconductivity induced in topological materials are briefly discussed. Topological insulators beyond the Z_2 classification such as Topological Crystalline Insulators (TCI) are discussed based on their spin properties (mirror Chern invariants). The experimental methodologies detailed here have been used in most of the subsequent studies of Z_2 topological physics in almost all bulk topological insulator materials to this date.

CONTENTS

I. Introduction 1

II. The birth of momentum-resolved spectroscopy as a direct experimental probe of Z_2 Topological-Order 2

III. Separation of insulating bulk from metallic surface states using incident photon energy modulated ARPES 4

IV. Winding number count: Counting of surface Fermi surfaces enclosing Kramers points to identify topologically non-trivial surface spin-textured states 6

V. Spin-resolving the surface states to identify the non-trivial topological phase and establish a 2D helical metal protected from backscattering 10

VI. Identifying the origin of 3D topological order via a bulk band gap inversion transition 12

VII. Topological protection and tunability of the surface states of a 3D topological insulator 18

VIII. Future directions: Topological Superconductors and Topological Crystalline Insulators 19

References 22

INTRODUCTION

The three-dimensional topological insulator (originally called "topological insulators" to distinguish this novel state from all types of quantum Hall and spin Hall-like effects since the original quantum Hall state is the time-reversal breaking 2D topological insulator first discovered in 1980) is the first (and only known experimental) example in nature of a topologically ordered electronic phase existing in bulk solids. Their topological order can be realized at room temperatures without magnetic fields and they can be turned into magnets and exotic superconductors leading to world-wide interest and activity in topological insulators [1–8]. All of the 2D topological insulator examples (Integer Quantum Hall(IQH), Quantum Spin Hall(QSH)) including the fractional one (FQH) involving Coulomb interaction are understood in the standard picture of quantized electron orbits in a spin-independent or spin-dependent magnetic field, the 3D topological insulator defies such description and is a novel type of topological order which cannot be reduced to multiple copies of quantum-Hall-like states. In fact, the 3D topological insulator exists not only in zero magnetic field but differs from the 2D variety in three very important aspects: **1**) they possess topologically protected 2D metallic surfaces (Topological Sur-

face States, a new type of 2DEG) rather than the 1D edges, **2**) they can work at room temperature (300K and beyond) rather than cryogenic (sub-K) temperatures required for the QSH effects and **3**) they occur in standard bulk semiconductors rather than at buried interfaces of ultraclean semiconductor heterostructures and thus tolerate stronger disorder than the IQH-like states. One of the major challenges in going from quantum Hall-like 2D states to 3D topological insulators is to employ new experimental approaches/methods to precisely probe this novel form of topological-order since the standard tools and settings that work for IQH-states also work for QSH states. The method to probe 2D topological-order is exclusively with charge transport. In a 3D topological insulator, the boundary itself supports a 2DEG and transport is not (Z_2) topologically quantized hence *cannot* directly probe the topological invariants ν_o nor the topological quantum numbers analogous to the Chern numbers of the IQH systems. This is *unrelated* to the fact that the present materials have some extrinsic or residual/impurity conductivity in their naturally grown bulk. In this paper, we review the birth of momentum- and spin-resolved spectroscopy as a new experimental approach and as a highly boundary sensitive method to study and prove topological-order via the direct measurements of the topological invariants ν_o that are associated with the Z_2 topology of the spin-orbit band structure and opposite parity band inversions. These experimental methods led to the experimental discovery of the first 3D topological insulator in Bi-Sb semiconductors which further led to the discovery of the Bi_2Se_3 class - the most widely researched topological insulator to this date. We discuss the fundamental properties of the novel topologically spin-momentum locked half Dirac metal on the surfaces of the topological insulators and how they emerge from topological phase transitions due to increasing spin-orbit coupling in the bulk. These methods and their derivatives are now being applied by others world-wide for further finer investigations of topological-order and for discovering new topological insulator states as well as exotic topological quantum phenomena. We also review how spectroscopic methods are leading to the identification of spin-orbit superconductors that may work as Majorana platforms and can be used to identify topological superconductors - yet another class of new states of matter.

THE BIRTH OF MOMENTUM-RESOLVED SPECTROSCOPY AS A DIRECT EXPERIMENTAL PROBE OF Z_2 TOPOLOGICAL-ORDER

Ordered phases of matter such as a superfluid or a ferromagnet are usually associated with the breaking of a symmetry and are characterized by a local order parameter [9]. The typical experimental probes of these systems are sensitive to order parameters. In the 1980s, two new phases of matter were realized by subjecting 2D electron gases at buried interfaces of semiconductor heterostructures to large magnetic fields. These new phases of matter, the 2D integer and 2D fractional quantum Hall states, exhibited a new and rare type of order that is derived from an organized collective quantum entangled motion of electrons [10–13]. These so-called "2D topologically ordered insulators" do not exhibit any symmetry breaking and are characterized by a topological number [14] as opposed to a local order parameter. The most striking manifestation of this 2D topological order is the existence of one-way propagating 1D metallic states confined to their edges, which lead to remarkable quantized charge transport phenomena. To date the experimental probe of their topological quantum numbers is based on charge transport, where measurements of the quantization of transverse magneto-conductivity $\sigma_{xy} = ne^2/h$ (where e is the electric charge and h is Planck's constant) reveals the value of the topological number n that characterizes these quantum Hall states [15].

Recently, a third type of 2D topological insulator, the spin quantum Hall insulator, was theoretically predicted [16, 17] and then experimentally discovered [18]. This class of quantum Hall-like topological phases can exist in spin-orbit materials without external magnetic fields, and can be described as an ordinary quantum Hall state in a spin-dependent magnetic field. Their topological order gives rise to counter-propagating 1D edge states that carry opposite spin polarization, often described as a superposition of a spin up and spin down quantum Hall edge state (Figure 1). Like conventional quantum Hall systems, the 2D spin quantum Hall insulator (QSH) is realized at a buried solid interface. The first realization of this phase was made in (Hg,Cd)Te quantum wells using *charge transport* by measuring a longitudinal conductance of about $2e^2/h$ at mK temperatures [18]. The quantum spin Hall state can be thought of as two copies of integer quantum Hall states (IQH) and are protected by a Z_2 invariant.

It was also realized that a fundamentally new type of genuinely three-dimensional topological order might be realized in bulk crystals without need for an external magnetic field [7, 19, 20]. Such a 3D topological insulator cannot be reduced to multiple copies of the IQH and such phases would be only the fourth type of topologically ordered phase to be discovered in nature, and the first type to fall outside the quantum Hall-like 2D topological states (IQH, FQH, QSH). Instead of having quantum-Hall type 1D edge states, these so-called 3D topological insulators would possess unconventional metallic 2D topological surface states called spin-textured helical metals, a type of 2D electron gas long thought to be impossible to realize. However, it was recognized that 3D topological insulators would NOT necessarily exhibit a topologically (Z_2) quantized charge transport by themselves as carried out in the conventional transport settings of all quantum-Hall-like measurements. Therefore, their 3D topological quantum numbers (Z_2), the analogues of n (Chern num-

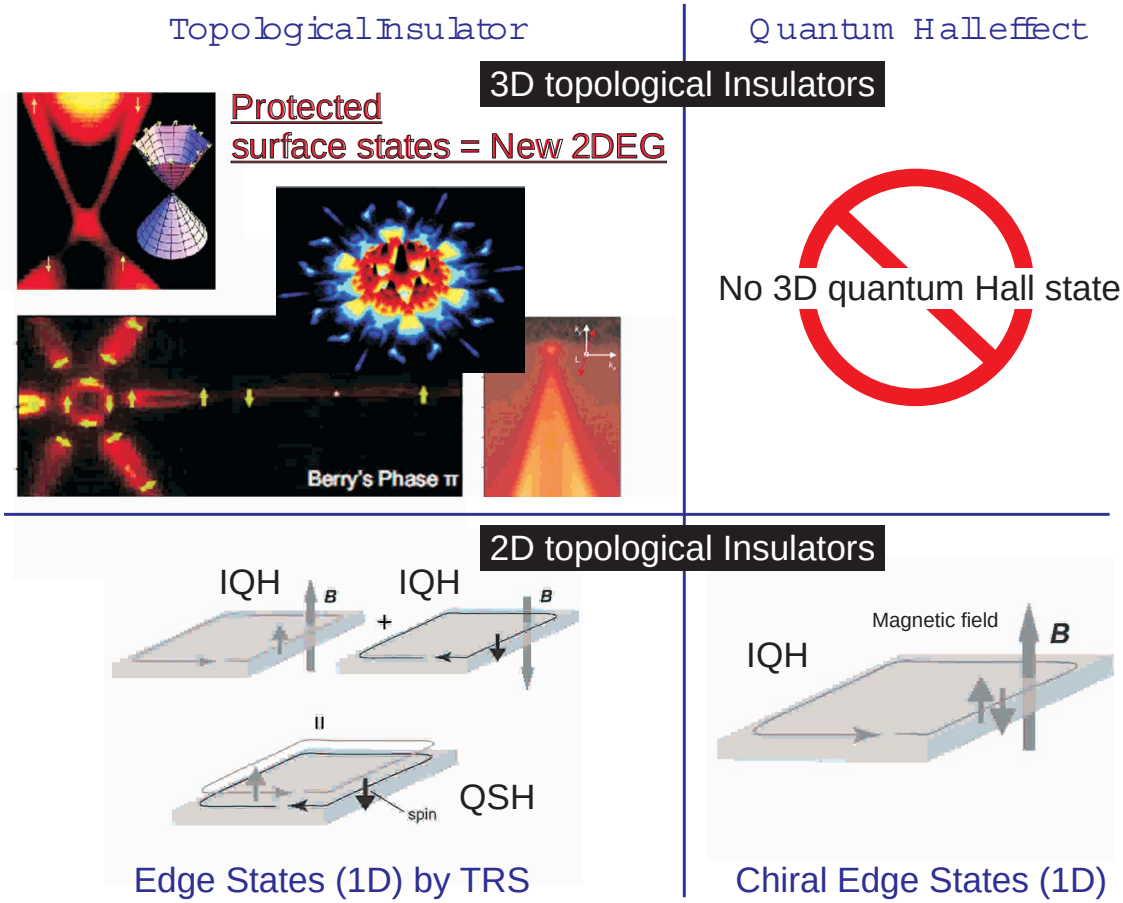


FIG. 1. **2D and 3D topological insulators in nature.** The 2D topological insulator class consists of the 2D quantum Hall states (IQH) and 2D quantum spin Hall state (QSH). The latter is constructed from two copies of the former. On the other hand, a 3D quantum Hall state is forbidden in nature, so the 3D topological insulator represents a new type of topologically ordered phase. The protected surface states form a novel type of topological metal (half Dirac metal) where electron's spin is locked to its momentum but exhibit no spin quantum Hall effect [1–8]

bers), could not be measured via the charge transport based methods even if a complete isolation of surface charge transport becomes routinely possible. Owing to the 2D nature of the two surface conduction channels (top and bottom surfaces of a typical thin sample) that contribute together in a 3D topological insulator case, it was theoretically recognized that it would not be possible to measure the topological invariants due to the lack of a quantized transport response of the 2D surface that measures the Z_2 topological invariants [20].

Here we review the development of spin- and angle-resolved photoemission spectroscopy (spin-ARPES) as the new approach/method to probe 3D topological order [21–35, 37], which today constitutes the experimental standard for identifying topological order in bulk solids. 3D topological insulators are also experimentally studied by many others world-wide using various techniques such as ARPES [36, 39–45], scanning tunneling spectroscopies (STM) [46–53], transport [54–65], optical methods [66**?** –73] and even on nano-structured samples [39, 56, 57]. Here, we will review the procedures for i) separating intrinsic bulk bands from surface electronic structures using incident photon energy modulated ARPES, ii) mapping the surface electronic structure across the Kramers momenta to establish the topologically non-trivial nature of the surface states, iii) using spin-ARPES to map the spin texture of the surface states to reveal topological quantum numbers and Berry's phases and iv) measuring the topological parent compounds to establish the microscopic origins of 3D topological order. These will be discussed in the context of $Bi_{1-x}Sb_x$, which was the first 3D topological insulator to be experimentally discovered in nature and a textbook example of how this method is applied. The confluence of three factors, having a detailed spectroscopic procedure to measure 3D topological order, their discovery in fairly simple bulk semiconductors and being able to work at room temperatures, has led to worldwide efforts to study 3D topological physics and led to over 100 compounds being identified as 3D topological insulators to date.

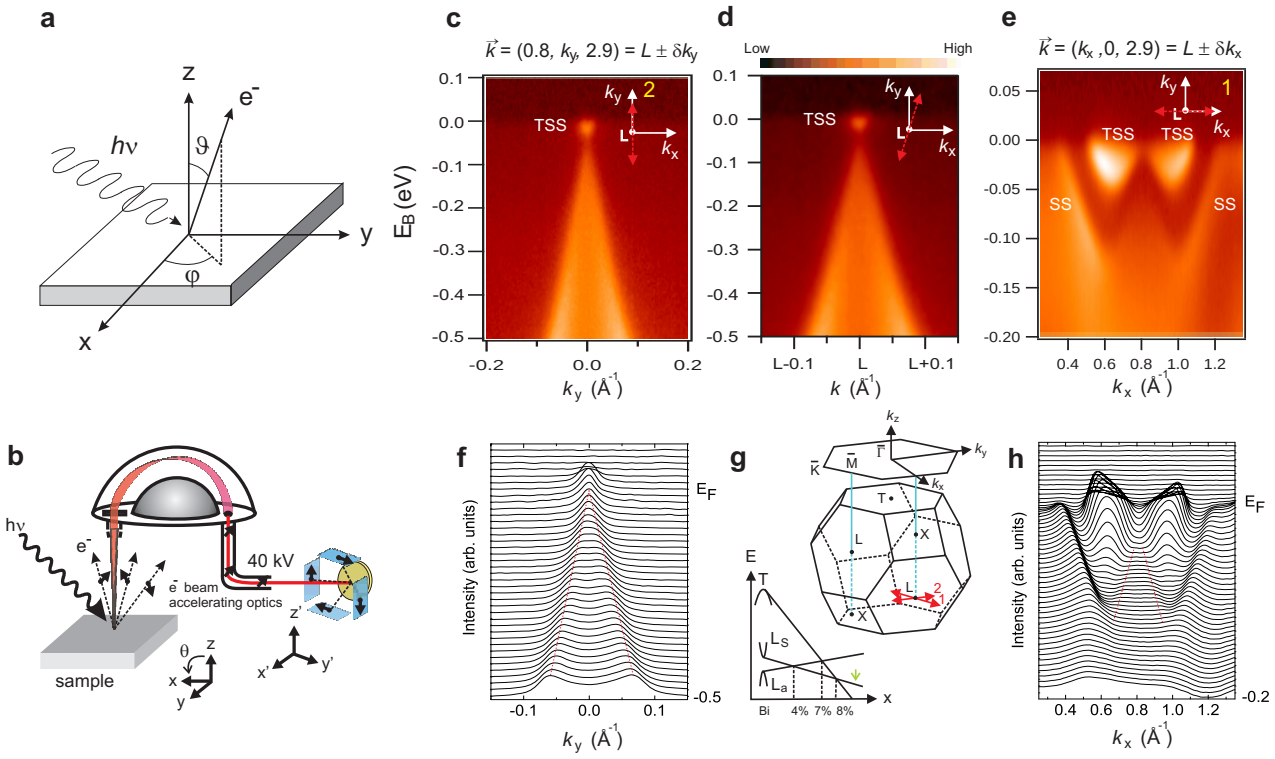


FIG. 2. **The first 3D topological insulator (2007) with in-gap Fermi level: Dirac-like dispersion signalling band inversion via spin-orbit interaction a**, Schematic of an ARPES experimental geometry. The kinetic energy of photoelectrons and their angles of emission (θ,ϕ) determine its electronic structure. **b**, Energy and momentum analysis take place through a hemispherical analyzer and the spin analysis is performed using a Mott detector. Selected ARPES intensity maps of $Bi_{0.9}Sb_{0.1}$ are shown along three $\vec{k}$-space cuts through the L point of the bulk 3D Brillouin zone (BZ). The presented data are taken in the third BZ with $L_z = 2.9$ $Å^{-1}$ with a photon energy of 29 eV. The cuts are along **c**, the k_y direction, **d**, a direction rotated by approximately 10° from the k_y direction, and **e**, the k_x direction. Each cut shows a Λ-shaped bulk band whose tip lies below the Fermi level signalling a bulk gap. The (topological) surface states are denoted (T)SS and are all identified in Fig.3. **f**, Momentum distribution curves (MDCs) corresponding to the intensity map in **c**. **h**, Log scale plot of the MDCs corresponding to the intensity map in **e**. The red lines are guides to the eye for the bulk features in the MDCs. **g**, Schematic of the bulk 3D BZ of $Bi_{1-x}Sb_x$ and the 2D BZ of the projected (111) surface. The high symmetry points $\bar{\Gamma}$, $\bar{M}$ and $\bar{K}$ of the surface BZ are labeled. Schematic evolution of bulk band energies as a function of x is shown. The L band inversion transition occurs at $x \approx 0.04$, where a 3D gapless Dirac point is realized, and the composition we study here (for which $x = 0.1$) is indicated by the green arrow. A more detailed phase diagram based on our experiments is shown in Fig.4c. Previous works on these compounds did not probe the topological aspects. [Adapted from D. Hsieh *et al.*, *Nature* **452**, 970 (2008) [Completed and submitted in **2007**] [21]].

SEPARATION OF INSULATING BULK FROM METALLIC SURFACE STATES USING INCIDENT PHOTON ENERGY MODULATED ARPES

Three-dimensional topological order is predicted to occur in semiconductors with an inverted band gap, therefore 3D topological insulators are often searched for in systems where a band gap inversion is known to take place as a function of some control parameter. The experimental signature of being in the vicinity of a bulk band inversion is that the bulk band dispersion should be described by the massive Dirac equation rather than Schr/"odinger equation, since the system must be described by the massless Dirac equation exactly at the bulk band inversion point.

The early theoretical treatments [19, 74] focused on the strongly spin-orbit coupled, band-inverted $Bi_{1-x}Sb_x$ series as a possible realization of 3D topological order for the following reason. Bismuth is a semimetal with strong spin-orbit interactions. Its band structure is believed to feature an indirect negative gap between the valence band maximum at the T point of the bulk Brillouin zone (BZ) and the conduction band minima at three equivalent L points [75, 76] (here we generally refer to these as a single point, L). The valence

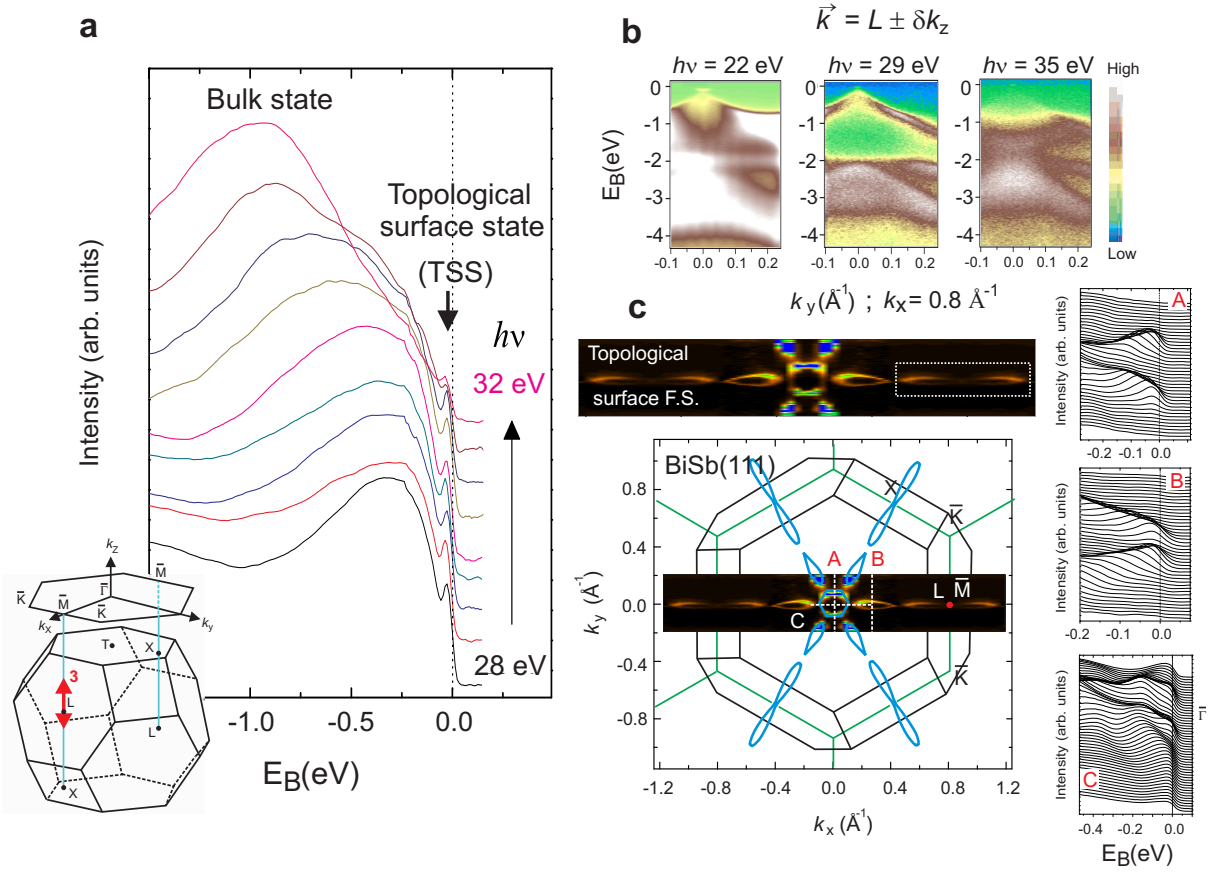


FIG. 3. **The first 3D topological insulator with in-gap Fermi level (2007): Topological Surface States and electronic band dispersion along the k_z-direction in momentum space.** Surface states are experimentally identified by studying their out-of-plane momentum dispersion through the systematic variation of incident photon energy. **a**, Energy distribution curves (EDCs) of $Bi_{0.9}Sb_{0.1}$ with electrons at the Fermi level (E_F) maintained at a fixed in-plane momentum of (k_x=0.8 Å^{-1}, k_y=0.0 Å^{-1}) are obtained as a function of incident photon energy to identify states that exhibit no dispersion perpendicular to the (111)-plane along the direction shown by the double-headed arrow labeled "3" in the inset. Selected EDC data sets with photon energies of 28 eV to 32 eV in steps of 0.5 eV are shown for clarity. The non-energy dispersive (k_z independent) peaks near E_F are the topological surface states (TSS). **b**, ARPES intensity maps along cuts parallel to k_y taken with electrons at E_F fixed at k_x = 0.8 Å^{-1} with respective photon energies of $h\nu$ = 22 eV, 29 eV and 35 eV. The faint Λ-shaped band at $h\nu$ = 22 eV and $h\nu$ = 35 eV shows some overlap with the bulk valence band at L ($h\nu$ = 29 eV), suggesting that it is a resonant surface state degenerate with the bulk state in some limited k-range near E_F. The flat band of intensity centered about −2 eV in the $h\nu$ = 22 eV scan originates from Bi 5d core level emission from second order light. **c**, Projection of the bulk BZ (black lines) onto the (111) surface BZ (green lines). Overlay (enlarged in inset) shows the high resolution Fermi surface (FS) of the metallic SS mode, which was obtained by integrating the ARPES intensity (taken with $h\nu$ = 20 eV) from −15 meV to 10 meV relative to E_F. The six tear-drop shaped lobes of the surface FS close to $\bar{\Gamma}$ (center of BZ) show some intensity variation between them that is due to the relative orientation between the axes of the lobes and the axis of the detector slit. The six-fold symmetry was however confirmed by rotating the sample in the $k_x - k_y$ plane. EDCs corresponding to the cuts A, B and C are also shown; these confirm the gapless character of the surface states in bulk insulating $Bi_{0.9}Sb_{0.1}$. [Adapted from D. Hsieh *et al.*, *Nature* **452**, 970 (2008) [21]].

and conduction bands at L are derived from antisymmetric (L_a) and symmetric (L_s) p-type orbitals, respectively, and the effective low-energy Hamiltonian at this point is described by the (3+1)-dimensional relativistic Dirac equation [77–79]. The resulting dispersion relation, $E(\vec{k}) = \pm\sqrt{(\vec{v})^2(\vec{k})^2 + \Delta^2} \approx \vec{v}\cdot\vec{k}$, is highly linear owing to the combination of an unusually large band velocity $\vec{v}$ and a small gap Δ (such that $|\Delta/|\vec{v}|| \approx 5\times10^{-3}$Å^{-1}) and has been used to explain various peculiar properties of bismuth [77–79]. Substituting bismuth with antimony is believed to change the critical energies of the band structure as follows (see Fig.2). At an Sb concentration of $x \approx 4\%$, the gap Δ between L_a and L_s closes and a massless three-dimensional (3D) Dirac point is realized. As x is further increased this gap re-opens with inverted

symmetry ordering, which leads to a change in sign of Δ at each of the three equivalent L points in the BZ. For concentrations greater than $x \approx 7\%$ there is no overlap between the valence band at T and the conduction band at L, and the material becomes an inverted-band insulator. Once the band at T drops below the valence band at L, at $x \approx 8\%$, the system evolves into a direct-gap insulator whose low energy physics is dominated by the spin-orbit coupled Dirac particles at L [19, 75].

High-momentum-resolution angle-resolved photoemission spectroscopy (Fig.2a & b) performed with varying incident photon energy (IPEM-ARPES) allows for measurement of electronic band dispersion along various momentum space ($\vec{k}$-space) trajectories in the 3D bulk BZ. ARPES spectra taken along two orthogonal cuts through the L point of the bulk BZ of $Bi_{0.9}Sb_{0.1}$ are shown in Figs 2 c and e. A Λ-shaped dispersion whose tip lies less than 50 meV below the Fermi energy (E_F) can be seen along both directions. Additional features originating from surface states that do not disperse with incident photon energy are also seen. Owing to the finite intensity between the bulk and surface states, the exact binding energy (E_B) where the tip of the Λ-shaped band dispersion lies is unresolved. The linearity of the bulk Λ-shaped bands is observed by locating the peak positions at higher E_B in the momentum distribution curves (MDCs), and the energy at which these peaks merge is obtained by extrapolating linear fits to the MDCs. Therefore 50 meV represents a lower bound on the energy gap Δ between L_a and L_s. The magnitude of the extracted band velocities along the k_x and k_y directions are $7.9 \pm 0.5 \times 10^4$ ms^{-1} and $10.0 \pm 0.5 \times 10^5$ ms^{-1}, respectively, which are similar to the tight binding values 7.6×10^4 ms^{-1} and 9.1×10^5 ms^{-1} calculated for the L_a band of bismuth [76]. Our data are consistent with the extremely small effective mass of $0.002m_e$ (where m_e is the electron mass) observed in magneto-reflection measurements on samples with $x = 11\%$ [80]. The Dirac point in graphene, coincidentally, has a band velocity ($|v_F| \approx 10^6$ ms^{-1}) [81] comparable to what we observe for $Bi_{0.9}Sb_{0.1}$, but its spin-orbit coupling is several orders of magnitude weaker, and the only known method of inducing a gap in the Dirac spectrum of graphene is by coupling to an external chemical substrate (which is a trivial gap) [82]. The $Bi_{1-x}Sb_x$ series thus provides a rare opportunity to study relativistic Dirac Hamiltonian physics in a 3D condensed matter system where the intrinsic (rest) mass gap can be easily tuned.

Studying the band dispersion perpendicular to the sample surface provides a way to differentiate bulk states from surface states in a 3D material. To visualize the near-E_F dispersion along the 3D L-X cut (X is a point that is displaced from L by a k_z distance of $3\pi/c$, where c is the lattice constant), in Fig.3a we plot energy distribution curves (EDCs), taken such that electrons at E_F have fixed in-plane momentum $(k_x, k_y) = (L_x, L_y) = (0.8$ Å^{-1}, 0.0 Å$^{-1})$, as a function of photon energy ($h\nu$). There are three prominent features in the EDCs: a non-dispersing, k_z independent, peak centered just below E_F at about -0.02 eV; a broad non-dispersing hump centered near -0.3 eV; and a strongly dispersing hump that coincides with the latter near $h\nu = 29$ eV. To understand which bands these features originate from, we show ARPES intensity maps along an in-plane cut $\bar{K}\bar{M}\bar{K}$ (parallel to the k_y direction) taken using $h\nu$ values of 22 eV, 29 eV and 35 eV, which correspond to approximate k_z values of $L_z -$ 0.3 Å^{-1}, L_z, and $L_z + 0.3$ Å^{-1} respectively (Fig.3b). At $h\nu = 29$ eV, the low energy ARPES spectral weight reveals a clear Λ-shaped band close to E_F. As the photon energy is either increased or decreased from 29 eV, this intensity shifts to higher binding energies as the spectral weight evolves from the Λ-shaped into a $\cup$-shaped band. Therefore the dispersive peak in Fig.2a comes from the bulk valence band, and for $h\nu = 29$ eV the high symmetry point L = (0.8, 0, 2.9) appears in the third bulk BZ. In the maps of Fig.3b with respective $h\nu$ values of 22 eV and 35 eV, overall weak features near E_F that vary in intensity remain even as the bulk valence band moves far below E_F. The survival of these weak features over a large photon energy range (17 to 55 eV) supports their surface origin. The non-dispersing feature centered near -0.3 eV in Fig.3a comes from the higher binding energy (valence band) part of the full spectrum of surface states, and the weak non-dispersing peak at -0.02 eV reflects the low energy part of the surface states that cross E_F away from the $\bar{M}$ point and forms the surface Fermi surface (Fig.3c).

WINDING NUMBER COUNT: COUNTING OF SURFACE FERMI SURFACES ENCLOSING KRAMERS POINTS TO IDENTIFY TOPOLOGICALLY NON-TRIVIAL SURFACE SPIN-TEXTURED STATES

Having established the existence of an energy gap in the bulk state of $Bi_{0.9}Sb_{0.1}$ (Figs 2 and 3) and observed linearly dispersive bulk bands uniquely consistent with strong spin-orbit coupling model calculations [76–79], we now discuss the topological character of its surface states, which are found to be gapless (Fig.3c). In general, the states at the surface of spin-orbit coupled compounds are allowed to be spin split owing to the loss of space inversion symmetry $[E(k,\uparrow) = E(-k,\uparrow)]$. However, as required by Kramers' theorem, this splitting must go to zero at the four time reversal invariant momenta (TRIM) in the 2D surface BZ. As discussed in [19, 20], along a path connecting two TRIM in the same BZ, the Fermi energy inside the bulk gap will intersect these singly degenerate surface states either an even or odd number of times. When there are an even number of surface state crossings, the surface states are topologically Z_2 trivial because disorder or correlations can remove *pairs* of such crossings by pushing the surface bands entirely above or below E_F. When there are an odd number of crossings, however, at least one surface state must remain gapless,

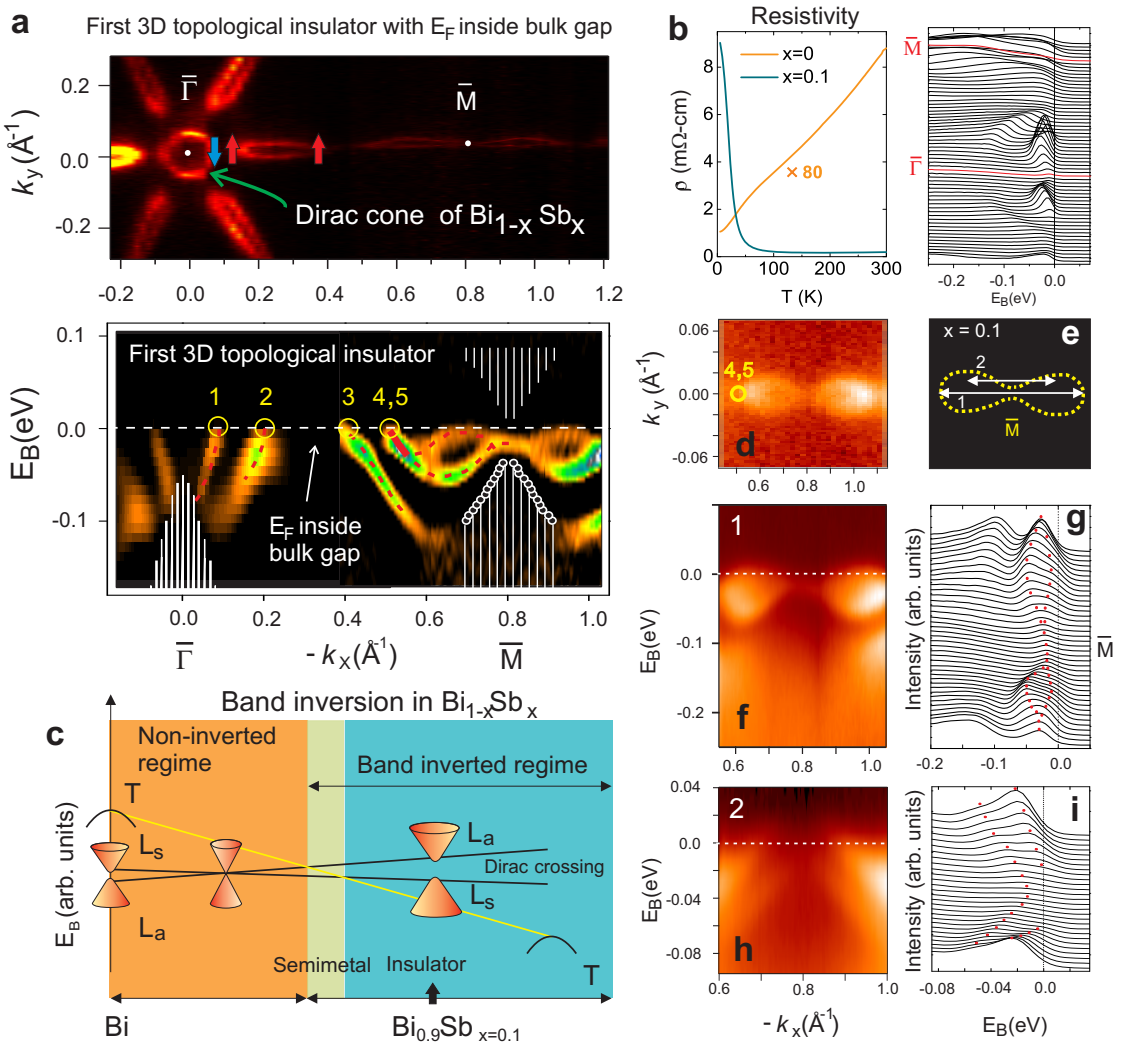


FIG. 4. **The first 3D topological insulator with in-gap Fermi level: The topological gapless surface states in bulk insulating (observed via the bulk band dispersion gap) $Bi_{0.9}Sb_{0.1}$. a**, The surface Fermi surface and surface band dispersion second derivative image (SDI) of $Bi_{0.9}Sb_{0.1}$ along $\bar{\Gamma}-\bar{M}$. The shaded white area shows the projection of the bulk bands based on ARPES data, as well as a rigid shift of the tight binding bands to sketch the unoccupied bands above the Fermi level. To maintain high momentum resolution, data were collected in two segments of momentum space, then the intensities were normalized using background level above the Fermi level. A non-intrinsic flat band of intensity near E_F generated by the SDI analysis was rejected to isolate the intrinsic dispersion. The Fermi crossings of the surface state are denoted by yellow circles, with the band near $-k_x \approx 0.5$ Å^{-1} counted twice owing to double degeneracy. The red lines are guides to the eye. An in-plane rotation of the sample by 60° produced the same surface state dispersion. The EDCs along $\bar{\Gamma}-\bar{M}$ are shown to the right. There are a total of five crossings from $\bar{\Gamma}-\bar{M}$ which indicates that these surface states are topologically non-trivial. The number of surface state crossings in a material (with an odd number of Dirac points) is related to the topological Z_2 invariant (see text). **b**, The resistivity curves of Bi and $Bi_{0.9}Sb_{0.1}$ reflect the contrasting transport behaviours. The presented resistivity curve for pure bismuth has been multiplied by a factor of 80 for clarity. **c**, Schematic variation of bulk band energies of $Bi_{1-x}Sb_x$ as a function of x (based on band calculations and on [19, 75]). $Bi_{0.9}Sb_{0.1}$ is a direct gap bulk Dirac point insulator well inside the inverted-band regime, and its surface forms a "topological metal" - the 2D analogue of the 1D edge states in quantum spin Hall systems. **d**, ARPES intensity integrated within ±10 meV of E_F originating solely from the surface state crossings. The image was plotted by stacking along the negative k_x direction a series of scans taken parallel to the k_y direction. **e**, Outline of $Bi_{0.9}Sb_{0.1}$ surface state ARPES intensity near E_F measured in **d**. White lines show scan directions "1" and "2". **f**, Surface band dispersion along direction "1" taken with $h\nu = 28$ eV and the corresponding EDCs (**g**). The surface Kramers degenerate point, critical in determining the topological Z_2 class of a band insulator, is clearly seen at $\bar{M}$, approximately 15 ± 5 meV below E_F. (We note that the scans are taken along the negative k_x direction, away from the bulk L point.) **h**, Surface band dispersion along direction "2" taken with $h\nu = 28$ eV and the corresponding EDCs (**i**). This scan no longer passes through the $\bar{M}$-point, and the observation of two well separated bands indicates the absence of Kramers degeneracy as expected, which cross-checks the result in (**a**). [Adapted from D. Hsieh *et al.*, *Nature* **452**, 970 (2008)[21]].

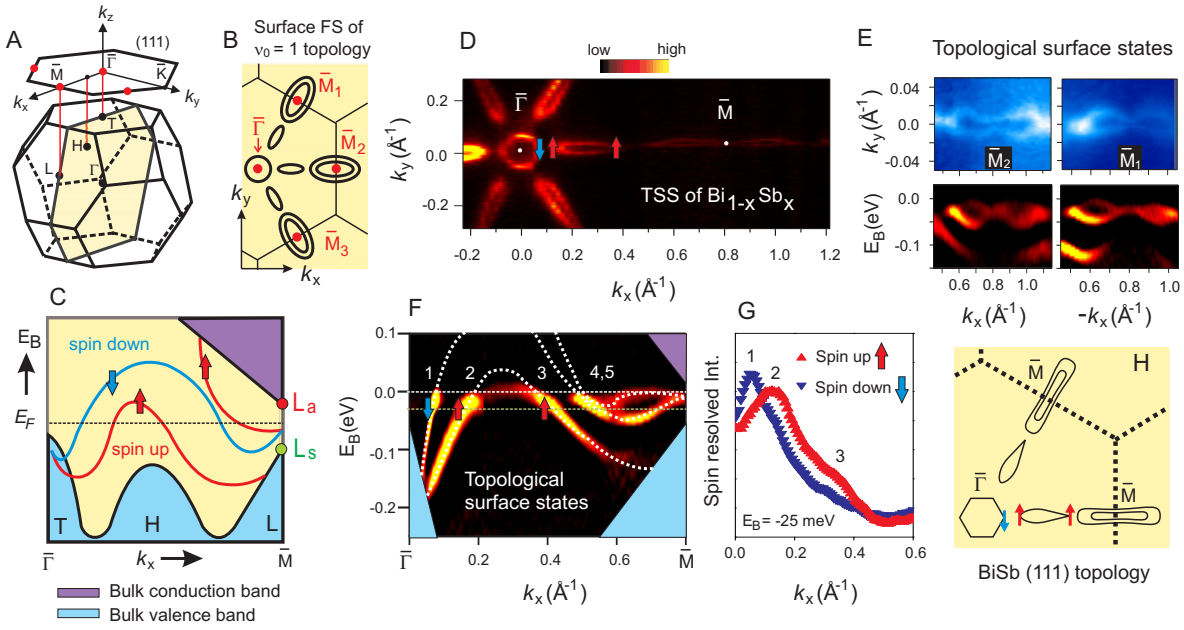


FIG. 5. **Spin texture of a topological insulator encodes Z_2 topological order of the bulk** (A) Schematic sketches of the bulk Brillouin zone (BZ) and (111) surface BZ of the $Bi_{1-x}Sb_x$ crystal series. The high symmetry points (L,H,T,Γ,$\bar{\Gamma}$,$\bar{M}$,$\bar{K}$) are identified. (B) Schematic of Fermi surface pockets formed by the surface states (SS) of a topological insulator that carries a Berry's phase. (C) Partner switching band structure topology: Schematic of spin-polarized SS dispersion and connectivity between $\bar{\Gamma}$ and $\bar{M}$ required to realize the FS pockets shown in panel-(B). L_a and L_s label bulk states at L that are antisymmetric and symmetric respectively under a parity transformation (see text). (D) Spin-integrated ARPES intensity map of the SS of $Bi_{0.91}Sb_{0.09}$ at E_F. Arrows point in the measured direction of the spin. (E) High resolution ARPES intensity map of the SS at E_F that enclose the $\bar{M}_1$ and $\bar{M}_2$ points. Corresponding band dispersion (second derivative images) are shown below. The left right asymmetry of the band dispersions are due to the slight offset of the alignment from the $\bar{\Gamma}$-$\bar{M}_1(\bar{M}_2)$ direction. (F) Surface band dispersion image along the $\bar{\Gamma}$-$\bar{M}$ direction showing five Fermi level crossings. The intensity of bands 4,5 is scaled up for clarity (the dashed white lines are guides to the eye). The schematic projection of the bulk valence and conduction bands are shown in shaded blue and purple areas. (G) Spin-resolved momentum distribution curves presented at $E_B = -25$ meV showing single spin degeneracy of bands at 1, 2 and 3. Spin up and down correspond to spin pointing along the $+\hat{y}$ and $-\hat{y}$ direction respectively. (H) Schematic of the spin-polarized surface FS observed in our experiments. It is consistent with a $\nu_0 = 1$ topology (compare (B) and (H)). [Adapted from D. Hsieh *et al.*, *Science* **323**, 919 (2009)[22]].

which makes it non-trivial [19, 20, 74]. The existence of such topologically non-trivial surface states can be theoretically predicted on the basis of the *bulk* band structure only, using the Z_2 invariant that is related to the quantum Hall Chern number [16]. Materials with band structures with $Z_2 = +1$ ($\nu_0 = 0$) are ordinary Bloch band insulators that are topologically equivalent to the filled shell atomic insulator, and are predicted to exhibit an even number (including zero) of surface state crossings. Materials with bulk band structures with $Z_2 = -1$ ($\nu_0 = 1$) on the other hand, which are expected to exist in rare systems with strong spin-orbit coupling acting as an internal quantizing magnetic field on the electron system [83], and inverted bands at an odd number of high symmetry points in their bulk 3D BZs, are predicted to exhibit an odd number of surface state crossings, precluding their adiabatic continuation to the atomic insulator [7, 17–20, 74]. Such "topological quantum Hall metals" [7, 20] cannot be realized in a purely 2D electron gas system such as the one realized at the interface of GaAs/GaAlAs systems.

In our experimental case, namely the (111) surface of $Bi_{0.9}Sb_{0.1}$, the four TRIM are located at $\bar{\Gamma}$ and three $\bar{M}$ points that are rotated by 60° relative to one another. Owing to the three-fold crystal symmetry (A7 bulk structure) and the observed mirror symmetry of the surface Fermi surface across $k_x = 0$ (Fig.3), these three $\bar{M}$ points are equivalent (and we henceforth refer to them as a single point, $\bar{M}$). The mirror symmetry $[E(k_y) = E(-k_y)]$ is also expected in this system. The complete details of the surface state dispersion observed in our experiments along a path connecting $\bar{\Gamma}$ and $\bar{M}$ are shown in Fig.4a; finding this information is made possible by our experimental separation of surface states from bulk states. As for bismuth (Bi), two surface bands emerge from the bulk band continuum near $\bar{\Gamma}$ to form a central electron pocket and an adjacent hole lobe [84–86]. It has been established that these two bands result from the spin-splitting of a surface state and are thus singly degenerate [86, 87]. On the other hand, the surface band that crosses E_F at $-k_x \approx 0.5$ Å^{-1}, and forms the narrow electron pocket

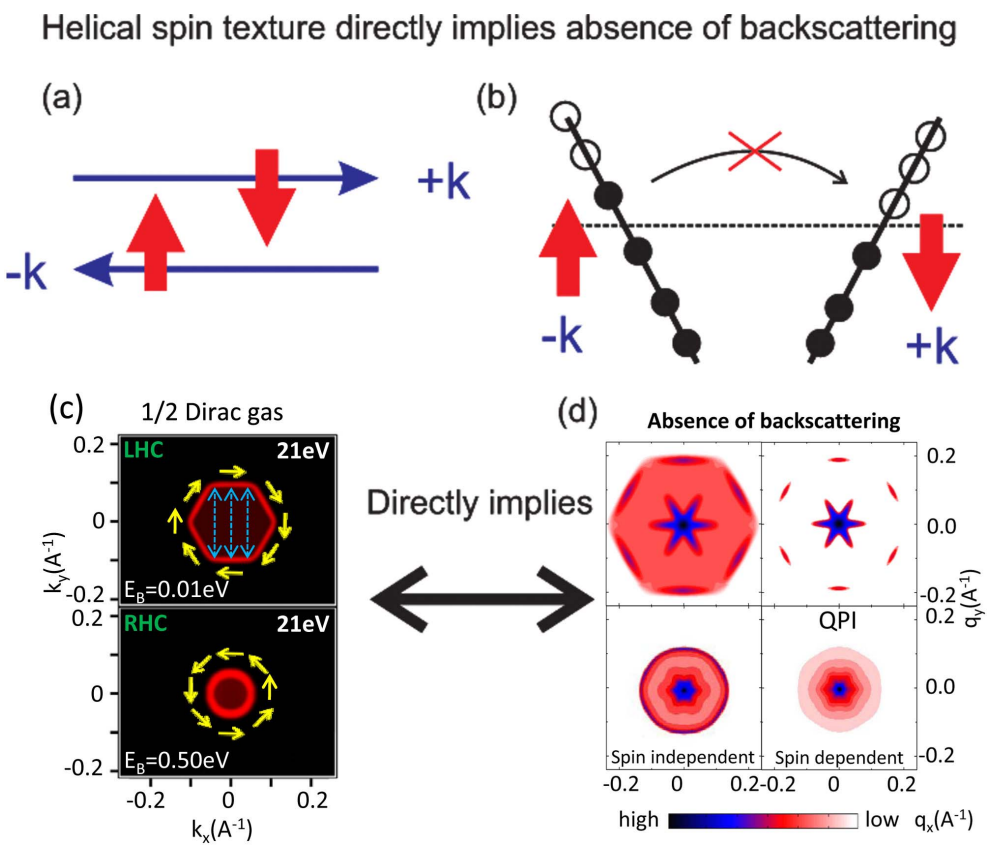


FIG. 6. **Helical spin texture naturally leads to absence of elastic backscattering for surface transport: No "U" turn on a 3D topological insulator surface.** (a) Our measurement of a helical spin texture in both $Bi_{1-x}Sb_x$ and in Bi_2Se_3 directly shows that there is (b) an absence of backscattering. (c) ARPES measured FSs are shown with spin directions based on polarization measurements. L(R)HC stands for left(right)-handed chirality. (d) Spin independent and spin dependent scattering profiles on FSs in (c) relevant for surface quasi-particle transport are shown which is sampled by the quasi-particle interference (QPI) modes. [Adapted from S.-Y. Xu *et al.*, *Science* **332** 560 (2011). [33]]

around $\bar{M}$, is clearly doubly degenerate, as far as we can determine within our experimental resolution. This is indicated by its splitting below E_F between $-k_x \approx 0.55$ $Å^{-1}$ and $\bar{M}$, as well as the fact that this splitting goes to zero at $\bar{M}$ in accordance with Kramers theorem. In semimetallic single crystal bismuth, only a single surface band is observed to form the electron pocket around $\bar{M}$ [88, 89]. Moreover, this surface state overlaps, hence becomes degenerate with, the bulk conduction band at L (L projects to the surface $\bar{M}$ point) owing to the semimetallic character of Bi (Fig.4b). In $Bi_{0.9}Sb_{0.1}$ on the other hand, the states near $\bar{M}$ fall completely inside the bulk energy gap preserving their purely surface character at $\bar{M}$ (Fig.4a). The surface Kramers doublet point can thus be defined in the bulk insulator (unlike in Bi [84–89]) and is experimentally located in $Bi_{0.9}Sb_{0.1}$ samples to lie approximately 15 ± 5 meV below E_F at $\vec{k} = \bar{M}$ (Fig.4a). For the precise location of this Kramers point, it is important to demonstrate that our alignment is strictly along the $\bar{\Gamma} - \bar{M}$ line. To do so, we contrast high resolution ARPES measurements taken along the $\bar{\Gamma} - \bar{M}$ line with those that are slightly offset from it (Fig.4e). Figs 4f-i show that with k_y offset from the Kramers point at $\bar{M}$ by less than 0.02 $Å^{-1}$, the degeneracy is lifted and only one band crosses E_F to form part of the bow-shaped electron distribution (Fig.4d). Our finding of five surface state crossings (an odd rather than an even number) between $\bar{\Gamma}$ and $\bar{M}$ (Fig.4a), confirmed by our observation of the Kramers degenerate point at the TRIM, indicates that these gapless surface states are topologically nontrivial. This corroborates our bulk electronic structure result that $Bi_{0.9}Sb_{0.1}$ is in the insulating band-inverted ($Z_2 = -1$ ($\nu_0 = 1$)) regime (Fig.4c), which contains an odd number of bulk (gapped) Dirac points.

These experimental results taken collectively strongly suggest that $Bi_{0.9}Sb_{0.1}$ is quite distinct from graphene [81, 90] and represents a novel state of quantum matter: a strongly spin-orbit coupled insulator with an odd number of Dirac points with a negative Z_2 topological Hall phase, which realizes the "parity anomaly without Fermion doubling". These works further demonstrates a general methodology for possible future investigations of *novel topological orders* in exotic quantum matter.

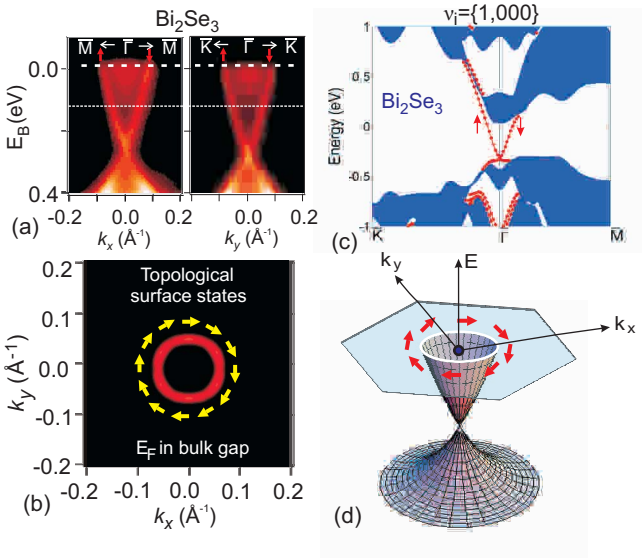


FIG. 7. **Spin-momentum locked helical fermions reveal topological-order of the bulk:** Spin-momentum locked helical surface Dirac fermions are hallmark signatures of topological insulators. (a) ARPES data for Bi_2Se_3 reveals surface electronic states with a single spin-polarized Dirac cone. The surface Fermi surface (b) exhibits a chiral left-handed spin texture. Data is from a sample doped to a Fermi level [thin line in (a)] that is in the bulk gap. ARPES measurements are carried out in P-polarizations mode which couples strongly to the (dominant) p_z orbital component of the surface state wavefunction. (c) Surface electronic structure of Bi_2Se_3 computed in the local density approximation. The shaded regions describe bulk states, and the red lines are surface states. (d) Schematic of the spin polarized surface state dispersion in the Bi_2X_3 topological insulators. [Adapted from Y. Xia *et al.*, *Nature Phys.* **5**, 398 (2009).[23]].

SPIN-RESOLVING THE SURFACE STATES TO IDENTIFY THE NON-TRIVIAL TOPOLOGICAL PHASE AND ESTABLISH A 2D HELICAL METAL PROTECTED FROM BACKSCATTERING

Strong topological materials are distinguished from ordinary materials such as gold by a topological quantum number, $\nu_0 = 1$ or 0 respectively [7, 16]. For $Bi_{1-x}Sb_x$, theory has shown that ν_0 is determined solely by the character of the bulk electronic wave functions at the L point in the three-dimensional (3D) Brillouin zone (BZ). When the lowest energy conduction band state is composed of an antisymmetric combination of atomic p-type orbitals (L_a) and the highest energy valence band state is composed of a symmetric combination (L_s), then $\nu_0 = 1$, and vice versa for $\nu_0 = 0$ [19]. Although the bonding nature (parity) of the states at L is not revealed in a measurement of the bulk band structure, the value of ν_0 can be determined from the spin-textures of the surface bands that form when the bulk is terminated. In particular, a $\nu_0 = 1$ topology requires the terminated surface to have a Fermi surface (FS) that supports a non-zero Berry's phase (odd as opposed to even multiple of π), which is not realizable in an ordinary spin-orbit material.

In a general inversion symmetric spin-orbit insulator, the bulk states are spin degenerate because of a combination of space inversion symmetry $[E(\vec{k},\uparrow) = E(-\vec{k},\uparrow)]$ and time reversal symmetry $[E(\vec{k},\uparrow) = E(-\vec{k},\downarrow)]$. Because space inversion symmetry is broken at the terminated surface, the spin degeneracy of surface bands can be lifted by the spin-orbit interaction [19-21]. However, according to Kramers theorem [16], they must remain spin degenerate at four special time reversal invariant momenta ($\vec{k}_T = \bar{\Gamma}$, $\bar{M}$) in the surface BZ [11], which for the (111) surface of $Bi_{1-x}Sb_x$ are located at $\bar{\Gamma}$ and three equivalent $\bar{M}$ points [see Fig.5(A)].

Depending on whether ν_0 equals 0 or 1, the Fermi surface pockets formed by the surface bands will enclose the four $\vec{k}_T$ an even or odd number of times respectively. If a Fermi surface pocket does not enclose $\vec{k}_T$ ($= \bar{\Gamma}$, $\bar{M}$), it is irrelevant for the Z_2 topology [19, 91]. Because the wave function of a single electron spin acquires a geometric phase factor of π [92] as it evolves by 360° in momentum space along a Fermi contour enclosing a $\vec{k}_T$, an odd number of Fermi pockets enclosing $\vec{k}_T$ in total implies a π geometrical (Berry's) phase [19]. In order to realize a π Berry's phase the surface bands must be spin-polarized and exhibit a partner switching [19] dispersion behavior between a pair of $\vec{k}_T$. This means that any pair of spin-polarized surface bands that are degenerate at $\bar{\Gamma}$ must not re-connect at $\bar{M}$, or must separately connect to the bulk valence and conduction band in between $\bar{\Gamma}$ and $\bar{M}$. The partner switching behavior is realized in Fig. 5(C) because the spin down band connects to and is degenerate with different spin up bands at $\bar{\Gamma}$ and $\bar{M}$.

We first investigate the spin properties of the topological insulator phase [22]. Spin-integrated ARPES [93] intensity maps of the (111) surface states of insulating $Bi_{1-x}Sb_x$ taken at the Fermi level (E_F) [Figs 5(D)&(E)] show that a hexagonal FS encloses $\bar{\Gamma}$, while dumbbell shaped FS pockets that are much weaker in intensity enclose $\bar{M}$. By examining the surface band dispersion below the Fermi level [Fig.5(F)] it is clear that the central hexagonal FS is formed by a single band (Fermi crossing 1) whereas the dumbbell shaped FSs are formed by the merger of two bands (Fermi crossings 4 and 5) [21].

This band dispersion resembles the partner switching dispersion behavior characteristic of topological insulators. To check this scenario and determine the topological index ν_0, we have carried out spin-resolved photoemission spectroscopy. Fig.5(G) shows a spin-resolved momentum distribution curve taken along the $\bar{\Gamma}$-$\bar{M}$ direction at a binding energy $E_B = -25$ meV [Fig.5(G)]. The data reveal a clear difference between the spin-up and spin-down intensities of bands 1, 2 and 3, and show that bands 1 and 2 have opposite spin whereas bands 2 and 3 have the same spin (detailed analysis discussed later

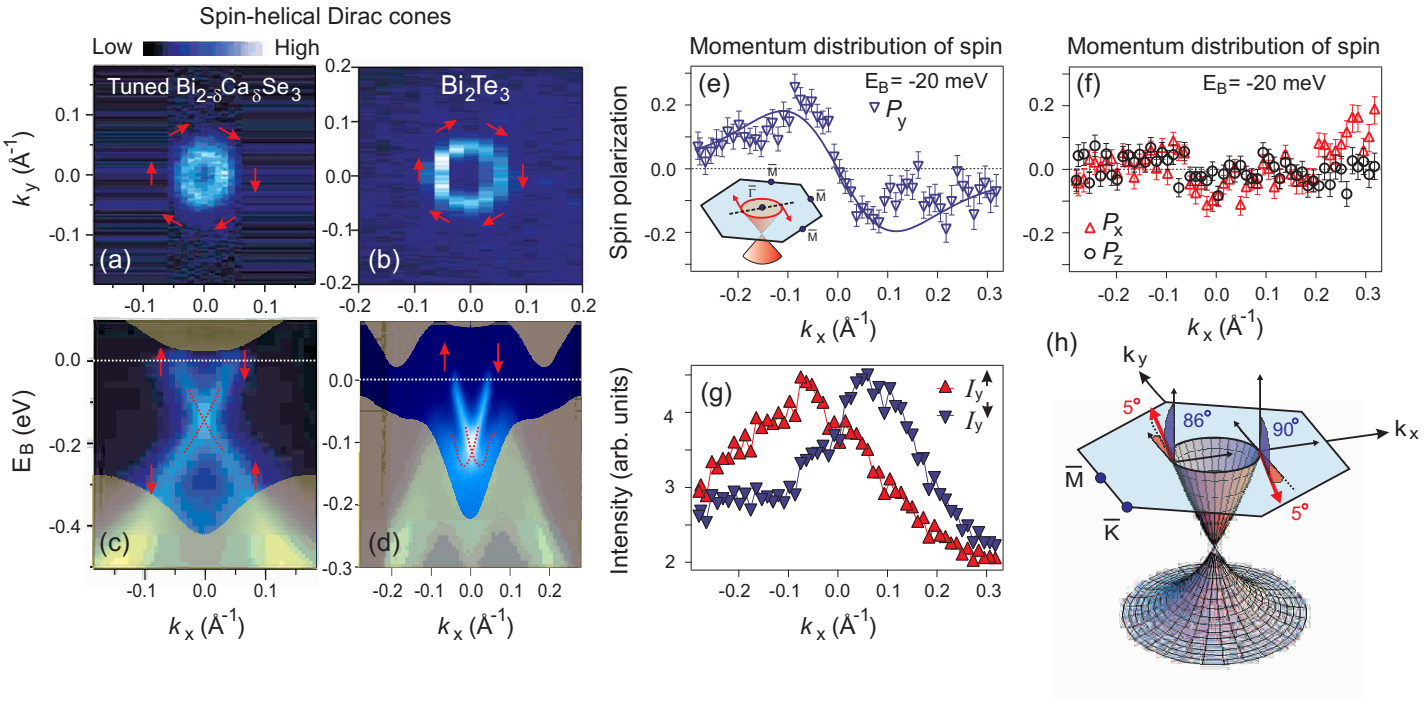


FIG. 8. **First detection of Topological-Order: spin-momentum locking of spin-helical Dirac electrons in Bi_2Se_3 and Bi_2Te_3 using spin-resolved ARPES.** (a) ARPES intensity map at E_F of the (111) surface of tuned $Bi_{2-\delta}Ca_\delta Se_3$ (see text) and (b) the (111) surface of Bi_2Te_3. Red arrows denote the direction of spin around the Fermi surface. (c) ARPES dispersion of tuned $Bi_{2-\delta}Ca_\delta Se_3$ and (d) Bi_2Te_3 along the k_x cut. The dotted red lines are guides to the eye. The shaded regions in (c) and (d) are our calculated projections of the bulk bands of pure Bi_2Se_3 and Bi_2Te_3 onto the (111) surface respectively. (e) Measured y component of spin-polarization along the $\bar{\Gamma}$-$\bar{M}$ direction at E_B = -20 meV, which only cuts through the surface states. Inset shows a schematic of the cut direction. (f) Measured x (red triangles) and z (black circles) components of spin-polarization along the $\bar{\Gamma}$-$\bar{M}$ direction at E_B = -20 meV. Error bars in (e) and (f) denote the standard deviation of $P_{x,y,z}$, where typical detector counts reach 5×10^5; Solid lines are numerical fits [94]. (g) Spin-resolved spectra obtained from the y component spin polarization data. The non-Lorentzian lineshape of the $I_y^{\uparrow}$ and $I_y^{\downarrow}$ curves and their non-exact merger at large $|k_x|$ is due to the time evolution of the surface band dispersion, which is the dominant source of statistical uncertainty. a.u., arbitrary units. (h) Fitted values of the spin polarization vector $\mathbf{P} = (S_x,S_y,S_z)$ are (sin(90°)cos(-95°), sin(90°)sin(-95°), cos(90°)) for electrons with $+k_x$ and (sin(86°)cos(85°), sin(86°)sin(85°), cos(86°)) for electrons with $-k_x$, which demonstrates the topological helicity of the spin-Dirac cone. ARPES measurements are carried out in P-polarizations mode which couples strongly to the (dominant) p_z orbital component of the surface state wavefunction. The angular uncertainties are of order ±10° and the magnitude uncertainty is of order ±0.15. [Adapted from D. Hsieh *et al.*, *Nature* **460**, 1101 (2009). [25]].

in text). The former observation confirms that bands 1 and 2 form a spin-orbit split pair, and the latter observation suggests that bands 2 and 3 (as opposed to bands 1 and 3) are connected above the Fermi level and form one band. This is further confirmed by directly imaging the bands through raising the chemical potential via doping. Irrelevance of bands 2 and 3 to the topology is consistent with the fact that the Fermi surface pocket they form does not enclose any $\vec{k}_T$. Because of a dramatic intrinsic weakening of signal intensity near crossings 4 and 5, and the small energy and momentum splitting of bands 4 and 5 lying at the resolution limit of modern spin-resolved ARPES spectrometers, no conclusive spin information about these two bands can be drawn from the methods employed in obtaining the data sets in Figs 5(G)&(H). However, whether bands 4 and 5 are both singly or doubly degenerate does not change the fact that an odd number of spin-polarized FSs enclose the $\vec{k}_T$, which provides evidence that $Bi_{1-x}Sb_x$ has ν_0 = 1 and that its surface supports a non-trivial Berry's phase. This directly implies an absence of backscattering in electronic transport along the surface (Fig.6), which has been re-confirmed by numerous scanning tunneling microscopy studies that show quasi-particle interference patterns that can only be modeled assuming an absence of backscattering [46–48].

Shortly after the discovery of $Bi_{1-x}Sb_x$, physicists sought to find a simpler version of a 3D topological insulator consisting of a single surface state instead of five. This is because the surface structure of $Bi_{1-x}Sb_x$ was rather complicated and the band gap was rather small. This motivated a search for topological insulators with a larger

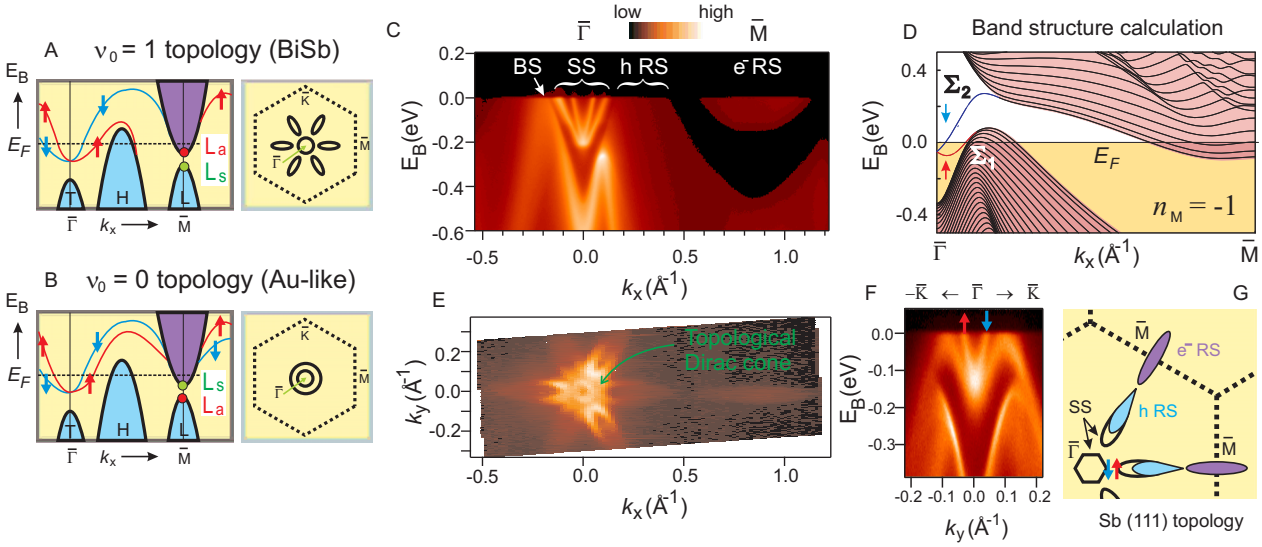


FIG. 9. **Topological character of parent compound revealed on the (111) surface states.** Schematic of the bulk band structure (shaded areas) and surface band structure (red and blue lines) of Sb near E_F for a (A) topologically non-trivial and (B) topological trivial (gold-like) case, together with their corresponding surface Fermi surfaces are shown. (C) Spin-integrated ARPES spectrum of Sb(111) along the $\bar{\Gamma}$-$\bar{M}$ direction. The surface states are denoted by SS, bulk states by BS, and the hole-like resonance states and electron-like resonance states by h RS and e$^-$ RS respectively. (D) Calculated surface state band structure of Sb(111) based on the methods in [76, 91]. The continuum bulk energy bands are represented with pink shaded regions, and the lines show the discrete bands of a 100 layer slab. The red and blue single bands, denoted Σ_1 and Σ_2, are the surface states bands with spin polarization $\langle \vec{P} \rangle \propto +\hat{y}$ and $\langle \vec{P} \rangle \propto -\hat{y}$ respectively. (E) ARPES intensity map of Sb(111) at E_F in the k_x-k_y plane. The only one FS encircling $\bar{\Gamma}$ seen in the data is formed by the inner V-shaped SS band seen in panel-(C) and (F). The outer V-shaped band bends back towards the bulk band best seen in data in panel-(F). (F) ARPES spectrum of Sb(111) along the $\bar{\Gamma} - \bar{K}$ direction shows that the outer V-shaped SS band merges with the bulk band. (G) Schematic of the surface FS of Sb(111) showing the pockets formed by the surface states (unfilled) and the resonant states (blue and purple). The purely surface state Fermi pocket encloses only one Kramers degenerate point ($\vec{k}_T$), namely, $\bar{\Gamma}(=\vec{k}_T)$, therefore consistent with the $\nu_0 = 1$ topological classification of Sb which is different from Au (compare (B) and (G)). As discussed in the text, the hRS and e$^-$RS count trivially. [Adapted from D. Hsieh *et al.*, *Science* **323**, 919 (2009) [22]].

band gap and simpler surface spectrum. A second generation of 3D topological insulator materials, especially Bi_2Se_3, offers the potential for topologically protected behavior in ordinary crystals at room temperature and zero magnetic field. Starting in 2008, work by the Princeton group used spin-ARPES and first-principles calculations to study the surface band structure of Bi_2Se_3 and observe the characteristic signature of a topological insulator in the form of a single Dirac cone that is spin-polarized (Figs 7 and 8) such that it also carries a non-trivial Berry's phase [23, 25]. Concurrent theoretical work by [24] used electronic structure methods to show that Bi_2Se_3 is just one of several new large band-gap topological insulators. These other materials were soon after also identified using this ARPES technique we describe [26, 27].

The Bi_2Se_3 surface state is found from spin-ARPES and theory to be a nearly idealized single Dirac cone as seen from the experimental data in Figs.7 and 16. An added advantage is that Bi_2Se_3 is stoichiometric (i.e., a pure compound rather than an alloy such as $Bi_{1-x}Sb_x$) and hence can be prepared, in principle, at higher purity. While the topological insulator phase is predicted to be quite robust to disorder, many experimental probes of the phase, including ARPES of the surface band structure, are clearer in high-purity samples. Finally and perhaps most important for applications, Bi_2Se_3 has a large band gap of around 0.3 eV (3600 K). This indicates that in its high-purity form Bi_2Se_3 can exhibit topological insulator behavior at room temperature and greatly increases the potential for applications, which we discuss in greater depth later in the review.

IDENTIFYING THE ORIGIN OF 3D TOPOLOGICAL ORDER VIA A BULK BAND GAP INVERSION TRANSITION

We investigated the quantum origin of topological order in the $Bi_{1-x}Sb_x$ and Bi_2Se_3 classes of materials. It has been theoretically speculated that the novel topological order in $Bi_{1-x}Sb_x$ originates from the parities of the electrons in pure Sb and not Bi [19, 75]. It was also noted [91] that the origin of the topological effects can only be tested by measuring the spin-texture of the Sb surface, which has not been measured. Based on quantum oscillation and magneto-optical studies, the bulk band structure of Sb is known to evolve from that of insulating $Bi_{1-x}Sb_x$ through the hole-like band at H rising above

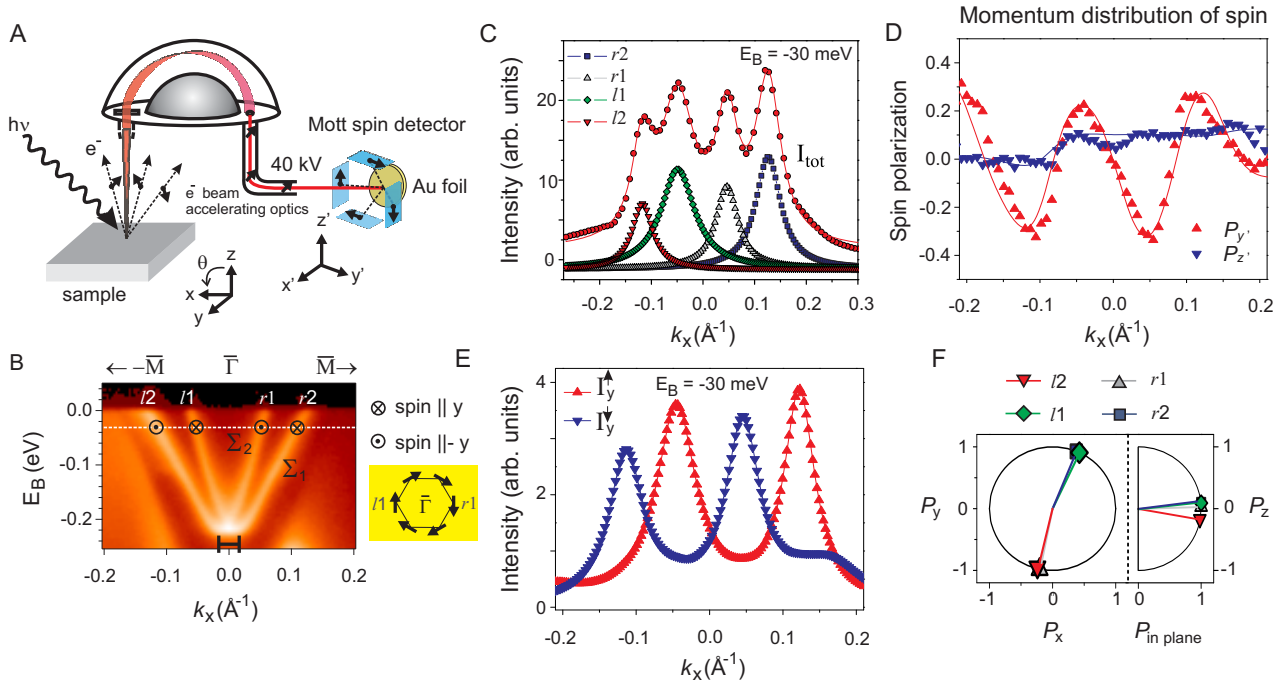


FIG. 10. **Spin-texture of topological surface states and topological chirality.** (A) Experimental geometry of the spin-resolved ARPES study. At normal emission ($\theta = 0°$), the sensitive y'-axis of the Mott detector is rotated by 45° from the sample $\bar{\Gamma}$ to $-\bar{M}$ ($\parallel -\hat{x}$) direction, and the sensitive z'-axis of the Mott detector is parallel to the sample normal ($\parallel \hat{z}$). (B) Spin-integrated ARPES spectrum of Sb(111) along the $-\bar{M}$-$\bar{\Gamma}$-$\bar{M}$ direction. The momentum splitting between the band minima is indicated by the black bar and is approximately 0.03 Å^{-1}. A schematic of the spin chirality of the central FS based on the spin-resolved ARPES results is shown on the right. (C) Momentum distribution curve of the spin averaged spectrum at $E_B = -30$ meV (shown in (B) by white line), together with the Lorentzian peaks of the fit. (D) Measured spin polarization curves (symbols) for the detector y' and z' components together with the fitted lines using the two-step fitting routine [100]. (E) Spin-resolved spectra for the sample y component based on the fitted spin polarization curves shown in (D). Up (down) triangles represent a spin direction along the $+(-)\hat{y}$ direction. (F) The in-plane and out-of-plane spin polarization components in the sample coordinate frame obtained from the spin polarization fit. Overall spin-resolved data and the fact that the surface band that forms the central electron pocket has $\langle \vec{P} \rangle \propto -\hat{y}$ along the $+k_x$ direction, as in (E), suggest a left-handed chirality (schematic in (B) and see text for details). [Adapted from D. Hsieh *et al.*, *Science* **323**, 919 (2009) [22]].

E_F and the electron-like band at L sinking below E_F [75]. The relative energy ordering of the L_a and L_s states in Sb again determines whether the surface state pair emerging from $\bar{\Gamma}$ switches partners [Fig.9(A)] or not [Fig.9(B)] between $\bar{\Gamma}$ and $\bar{M}$, and in turn determines whether they support a non-zero Berry's phase.

In a conventional spin-orbit metal such as gold, a free-electron like surface state is split into two parabolic spin-polarized sub-bands that are shifted in $\vec{k}$-space relative to each other [95]. Two concentric spin-polarized Fermi surfaces are created, one having an opposite sense of in-plane spin rotation from the other, that enclose $\bar{\Gamma}$. Such a Fermi surface arrangement, like the schematic shown in figure 9(B), does not support a non-zero Berry's phase because the $\vec{k}_T$ are enclosed an even number of times (2 for most known materials).

However, for Sb, this is not the case. Figure 9(C) shows a spin-integrated ARPES intensity map of Sb(111) from $\bar{\Gamma}$ to $\bar{M}$. By performing a systematic incident photon energy dependence study of such spectra, previously unavailable with He lamp sources [96], it is possible to identify two V-shaped surface states (SS) centered at $\bar{\Gamma}$, a bulk state located near $k_x = -0.25$ Å^{-1} and resonance states centered about $k_x = 0.25$ Å^{-1} and $\bar{M}$ that are hybrid states formed by surface and bulk states [93]. An examination of the ARPES intensity map of the Sb(111) surface and resonance states at E_F [Fig.9(E)] reveals that the central surface FS enclosing $\bar{\Gamma}$ is formed by the inner V-shaped SS only. The outer V-shaped SS on the other hand forms part of a tear-drop shaped FS that does *not* enclose $\bar{\Gamma}$, unlike the case in gold. This tear-drop shaped FS is formed partly by the outer V-shaped SS and partly by the hole-like resonance state. The electron-like resonance state FS enclosing $\bar{M}$ does not affect the determination of ν_0 because it must be doubly spin degenerate . Such a FS geometry [Fig.9(G)] suggests that the V-shaped SS pair may undergo a partner switching behavior expected in Fig.9(A). This behavior is most clearly seen in a cut taken along the $\bar{\Gamma} - \bar{K}$ direction since the top of the bulk valence band is well below E_F [Fig.9(F)] show-

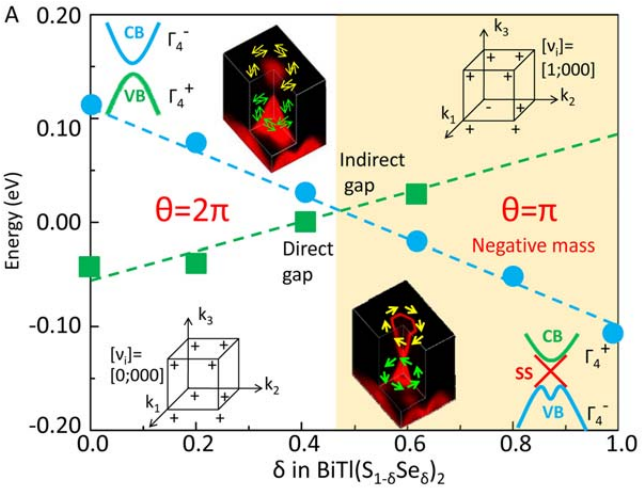


FIG. 11. **Observation of bulk band inversion across a topological quantum phase transition**. Energy levels of Γ_4^-. (blue circles) and Γ_4^+ (green squares) bands are obtained from ARPES measurements as a function of composition δ. CB: conduction band; VB: valence band. Parity eigenvalues (+ or) of Bloch states are shown. The topological invariants, ν_i, obtained from the parity eigenvalues are presented as $[\theta/\pi = \nu_0;\nu_1,\nu_2,\nu_3]$ where $\theta = \pi\nu_0$ is the axion angle [97] and ν_0 is the strong invariant. ARPES measurements are carried out in P-polarizations mode which couples strongly to the (dominant) p_z orbital component of the surface state wavefunction. [Adapted from S.-Y. Xu *et al.*, *Science* **332** 560 (2011). [33]]

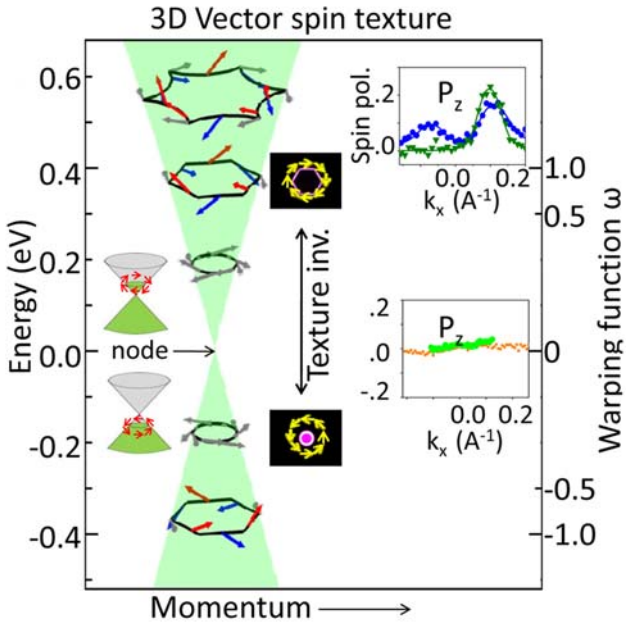


FIG. 12. **Spin texture evolution of topological surface bands as a function of energy away from the Dirac node** (left axis) and geometrical warping factor ω (right axis). The warping factor is defined as $\omega = \frac{k_F(\bar{\Gamma}-\bar{M})-k_F(\bar{\Gamma}-\bar{K})}{k_F(\bar{\Gamma}-\bar{M})+k_F(\bar{\Gamma}-\bar{K})} \times \frac{2+\sqrt{3}}{2-\sqrt{3}}$ where $\omega = 0$, $\omega = 1$, and $\omega > 1$ implies circular, hexagonal and snowflake-shaped FSs respectively. The sign of ω indicates texture chirality for LHC (+) or RHC (-). Insets: out-of-plane 3D spin-polarization measurements at corresponding FSs. ARPES measurements are carried out in P-polarizations mode which couples strongly to the (dominant) p_z orbital component of the surface state wavefunction. [Adapted from S.-Y. Xu *et al.*, *Science* **332** 560 (2011). [33]]

ing only the inner V-shaped SS crossing E_F while the outer V-shaped SS bends back towards the bulk valence band near $k_x = 0.1$ Å^{-1} before reaching E_F. The additional support for this band dispersion behavior comes from tight binding surface calculations on Sb [Fig.9(D)], which closely match with experimental data below E_F. Our observation of a single surface band forming a FS enclosing $\bar{\Gamma}$ suggests that pure Sb is likely described by $\nu_0 = 1$, and that its surface may support a Berry's phase.

Confirmation of a surface π Berry's phase rests critically on a measurement of the relative spin orientations (up or down) of the SS bands near $\bar{\Gamma}$ so that the partner switching is indeed realized, which cannot be done without spin resolution. Spin resolution was achieved using a Mott polarimeter that measures two orthogonal spin components of a photoemitted electron [98, 99]. These two components are along the y' and z' directions of the Mott coordinate frame, which lie predominantly in and out of the sample (111) plane respectively. Each of these two directions represents a normal to a scattering plane defined by the photoelectron incidence direction on a gold foil and two electron detectors mounted on either side (left and right) [Fig.10(A)]. Strong spin-orbit coupling of atomic gold is known to create an asymmetry in the scattering of a photoelectron off the gold foil that depends on its spin component normal to the scattering plane [99]. This leads to an asymmetry between

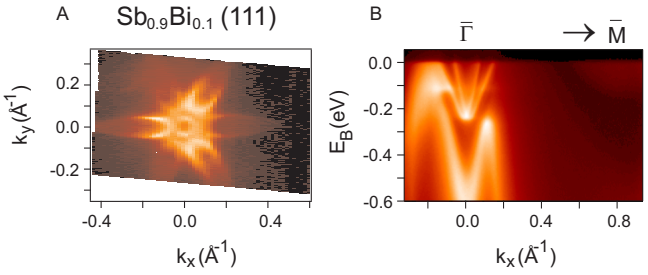


FIG. 13. **Robustness against disorder** Spin split surface states survive alloying disorder in $Sb_{0.9}Bi_{0.1}$. (**A**) ARPES intensity map at E_F of single crystal $Sb_{0.9}Bi_{0.1}$(111) in the k_x-k_y plane taken using 20 eV photons. (**B**) ARPES intensity map of $Sb_{0.9}Bi_{0.1}$(111) along the $\bar{\Gamma}$-$\bar{M}$ direction taken with $h\nu = 22$ eV photons. The band dispersion is not symmetric about $\bar{\Gamma}$ because of the three-fold rotational symmetry of the bulk states about the ⟨111⟩ axis. [Adapted from D. Hsieh *et al.*, *Science* **323**, 919 (2009) [22]].

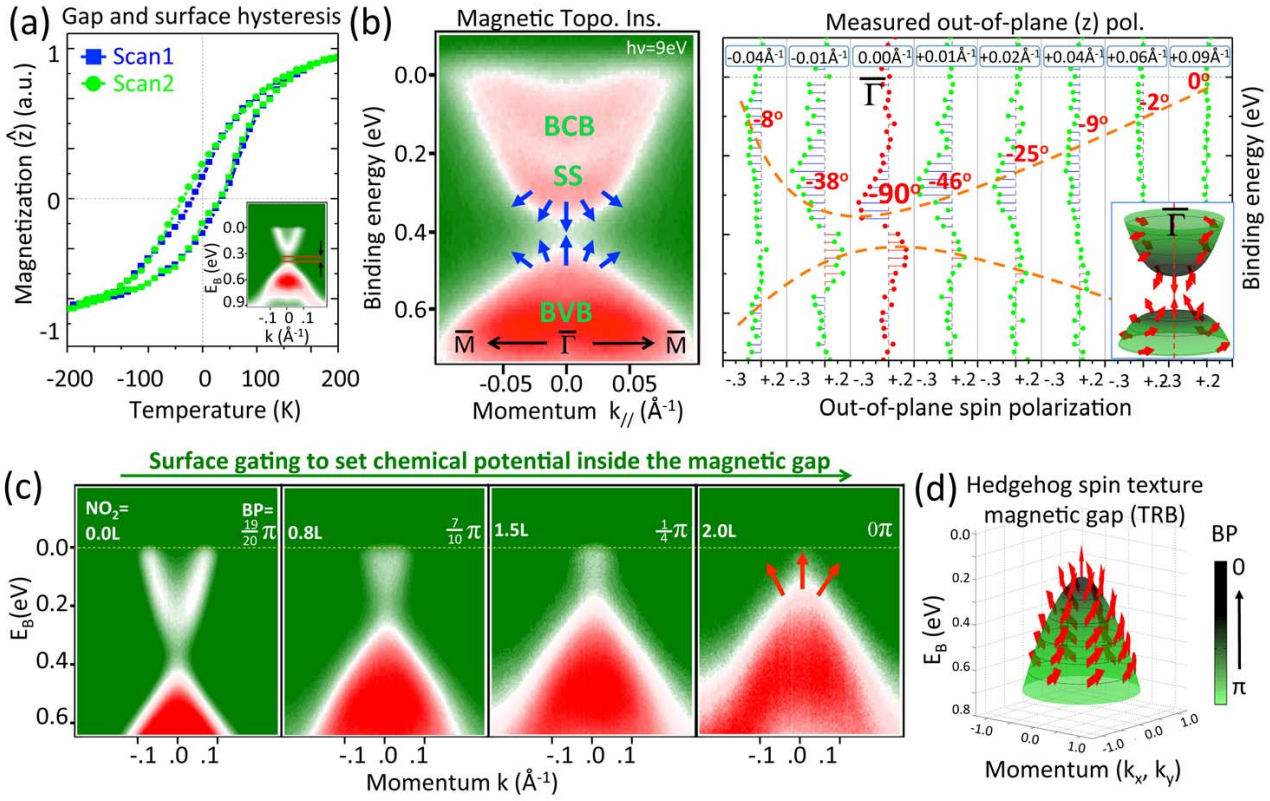


FIG. 14. **Hedgehog spin texture and Berry's phase tuning in a magnetic topological insulator.** (a) Magnetization measurements using magnetic circular dichroism shows out-of-plane ferromagnetic character of the Mn-Bi_2Se_3 MBE film surface through the observed hysteretic response. The inset shows the ARPES observed gap at the Dirac point in the Mn(2.5%)-Bi_2Se_3 film sample. (b) Spin-integrated and spin-resolved measurements on a representative piece of Mn(2.5%)-Bi_2Se_3 film sample using 9 eV photons. Left: Spin-integrated ARPES dispersion map. The blue arrows represent the spin texture configuration in close vicinity of the gap revealed by our spin-resolved measurements. Right, Measured out-of-plane spin polarization as a function of binding energy at different momentum values. The momentum value of each spin polarization curve is noted on the top. The polar angles (θ) of the spin polarization vectors obtained from these measurements are also noted. The 90° polar angle observed at $\bar{\Gamma}$ point suggests that the spin vector at $\bar{\Gamma}$ is along the vertical direction. The spin behavior at $\bar{\Gamma}$ and its surrounding momentum space reveals a hedgehog-like spin configuration for each Dirac band separated by the gap. Inset shows a schematic of the revealed hedgehog-like spin texture. (c) Measured surface state dispersion upon *in situ* NO_2 surface adsorption on the Mn-Bi_2Se_3 surface. The NO_2 dosage in the unit of Langmuir (1L = 1×10^{-6} torr·sec) and the tunable Berry's phase (BP) associated with the topological surface state are noted on the top-left and top-right corners of the panels, respectively. The red arrows depict the time-reversal breaking out-of-plane spin texture at the gap edge based on the experimental data. (d) The time-reversal breaking spin texture features a singular hedgehog-like configuration when the chemical potential is tuned to lie within the magnetic gap, corresponding to the experimental condition presented in the last panel in panel (c). [Adapted from S.-Y. Xu *et al.*, *Nature Physics* **8**, 616 (2012). [35]].

the left intensity ($I^L_{y',z'}$) and right intensity ($I^R_{y',z'}$) given by $A_{y',z'} = (I^L_{y',z'} - I^R_{y',z'})/(I^L_{y',z'} + I^R_{y',z'})$, which is related to the spin polarization $P_{y',z'} = (1/S_{eff}) \times A_{y',z'}$ through the Sherman function $S_{eff} = 0.085$ [98, 99]. Spin-resolved momentum distribution curve data sets of the SS bands along the $-\bar{M} - \bar{\Gamma} - \bar{M}$ cut at $E_B = -30$ meV [Fig.10(B)] are shown for maximal intensity. Figure 10(D) displays both y' and z' polarization components along this cut, showing clear evidence that the bands are spin polarized, with spins pointing largely in the (111) plane. In order to estimate the full 3D spin polarization vectors from a two component measurement (which is not required to prove the partner switching or the Berry's phase), we fit a model polarization curve to our data following the recent demonstration in Ref-[100], which takes the polarization directions associated with each momentum distribution curve peak [Fig.10(C)] as input parameters, with the constraint that each polarization vector has length one (in angular momentum units of $\hbar/2$). Our fitted polarization vectors are displayed in the sample (x, y, z) coordinate frame [Fig.10(F)], from which we derive the spin-resolved momentum distribution curves for the spin components parallel ($I^{\uparrow}_y$) and anti-parallel ($I^{\downarrow}_y$) to the y direction as shown in figure 10(E). There is a clear difference in $I^{\uparrow}_y$ and $I^{\downarrow}_y$ at each of the four momen-

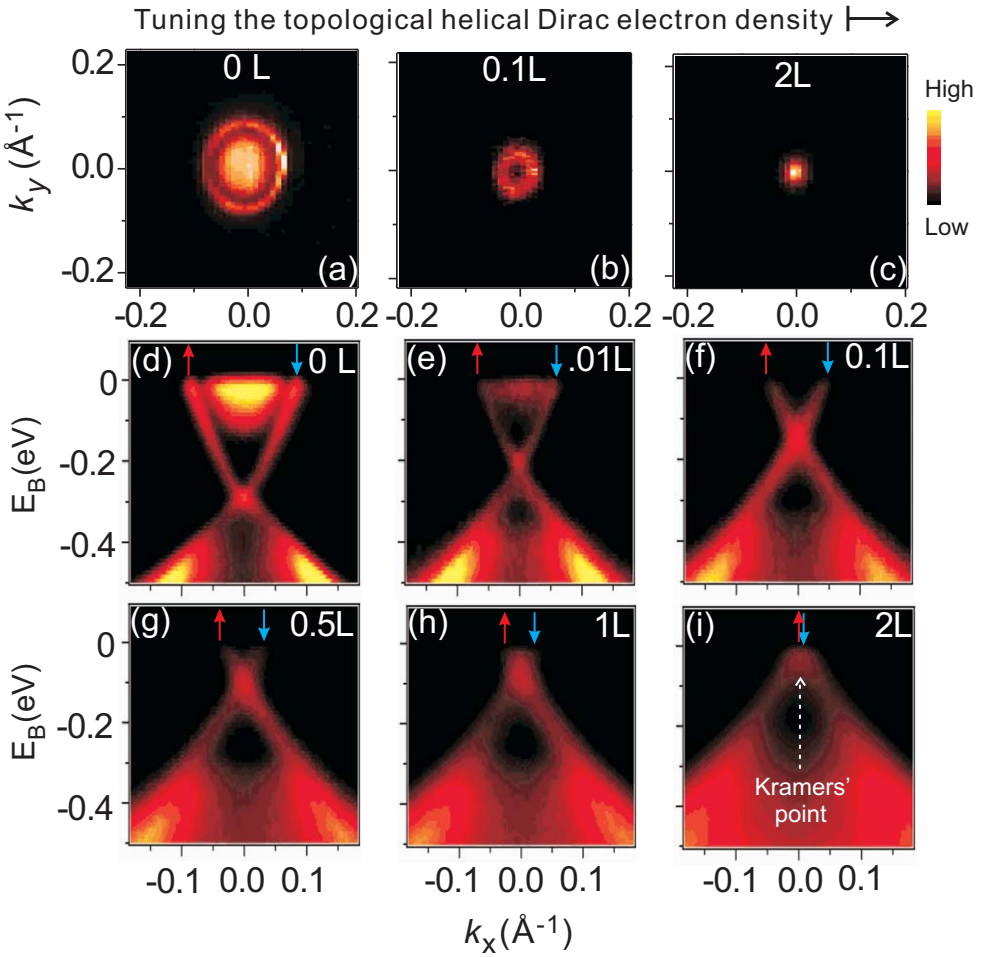


FIG. 15. **Surface Gating : Tuning the density of helical Dirac electrons to the spin-degenerate Kramers point and topological transport regime.** (a) A high resolution ARPES mapping of the surface Fermi surface (FS) near $\bar{\Gamma}$ of $Bi_{2-\delta}Ca_\delta Se_3$ (111). The diffuse intensity within the ring originates from the bulk-surface resonance state [7]. (b) The FS after 0.1 Langmuir (L) of NO_2 is dosed, showing that the resonance state is removed. (c) The FS after a 2 L dosage, which achieves the Dirac charge neutrality point. (d) High resolution ARPES surface band dispersions through after an NO_2 dosage of 0 L, (e) 0.01 L, (f) 0.1 L, (g) 0.5 L, (h) 1 L and (i) 2 L. The arrows denote the spin polarization of the bands. We note that due to an increasing level of surface disorder with NO_2 adsorption, the measured spectra become progressively more diffuse and the total photoemission intensity from the buried $Bi_{2-\delta}Ca_\delta Se_3$ surface is gradually reduced. [Adapted from D. Hsieh *et al.*, *Nature* **460**, 1101 (2009). [25]].

tum distribution curve peaks indicating that the surface state bands are spin polarized [Fig.10(E)], which is possible to conclude even without a full 3D fitting. Each of the pairs $l2/l1$ and $r1/r2$ have opposite spin, consistent with the behavior of a spin split pair, and the spin polarization of these bands are reversed on either side of $\bar{\Gamma}$ in accordance with the system being time reversal symmetric $[E(\vec{k},\uparrow) = E(-\vec{k},\downarrow)]$ [Fig.10(F)]. The measured spin texture of the Sb(111) surface states (Fig.10), together with the connectivity of the surface bands (Fig.9), uniquely determines its belonging to the $\nu_0 = 1$ class. Therefore the surface of Sb carries a non-zero (π) Berry's phase via the inner V-shaped band and pure Sb can be regarded as the parent metal of the $Bi_{1-x}Sb_x$ topological insulator class, in other words, the topological order originates from the Sb wave functions. A recent work [33] has demonstrated a topological quantum phase transition as a function of chemical composition from a non-inverted to an inverted semiconductor as a clear example of the origin of topological order (Fig.11).

Our spin polarized measurement methods (Fig.5 and 10) uncover a new type of topological quantum number n_M, which is not related to the time-reversal symmetry, but a consequence of the mirror symmetries of a crystalline system [91]. Topological band theory suggests that the bulk electronic states in the mirror ($k_y = 0$) plane can be classified in terms of a number n_M (=integer) [91], which defines both the number and the chirality of the spin helical edge states propagating along the mirror planes of a crystal.

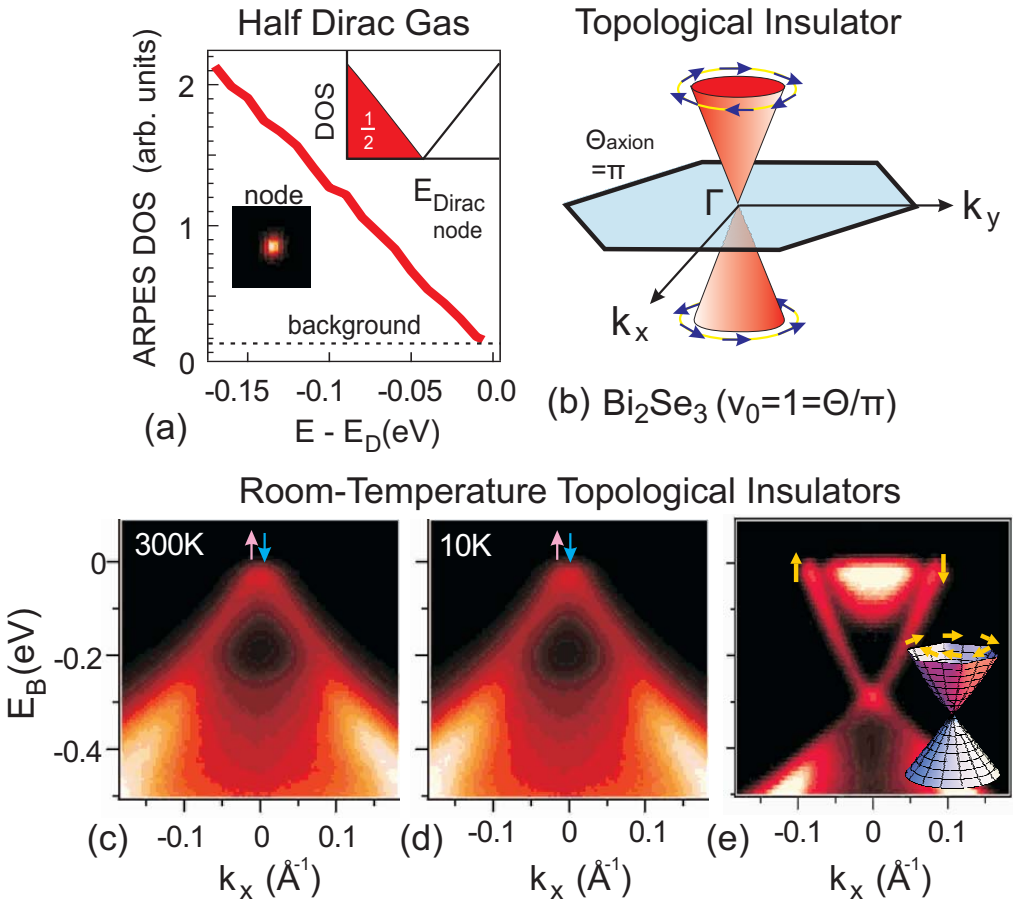


FIG. 16. **Observation of room temperature (300K) topological order without applied magnetic field in Bi_2Se_3:** (a) Crystal momentum integrated ARPES data near Fermi level exhibit linear fall-off of density of states, which, combined with the spin-resolved nature of the states, suggest that a half Fermi gas is realized on the topological surfaces. (b) Spin texture map based on spin-ARPES data suggest that the spin-chirality changes sign across the Dirac point. (c) The Dirac node remains well defined up a temperature of 300 K suggesting the stability of topological effects up to the room temperature. (d) The Dirac cone measured at a temperature of 10 K. (e) Full Dirac cone. [Adapted from D. Hsieh *et al.*, *Nature* **460**, 1101 (2009). [25]].

For example, we now determine the value of n_M of antimony surface states from our data. From figure 5, it is seen that a single (one) surface band, which switches partners at $\bar{M}$, connects the bulk valence and conduction bands, so $|n_M| = 1$. The sign of n_M is related to the direction of the spin polarization $\langle \vec{P} \rangle$ of this band [91], which is constrained by mirror symmetry to point along $\pm\hat{y}$. Since the central electron-like FS enclosing $\bar{\Gamma}$ intersects six mirror invariant points [see Fig.10(B)], the sign of n_M distinguishes two distinct types of handedness for this spin polarized FS. Figures 5(F) and 10 show that for both $Bi_{1-x}Sb_x$ and Sb, the surface band that forms this electron pocket has $\langle \vec{P} \rangle \propto -\hat{y}$ along the k_x direction, suggesting a left-handed rotation sense for the spins around this central FS thus $n_M = -1$. We note that similar analysis regarding the mirror symmetry and mirror eigenvalues $n_M = -1$ can be applied to the single Dirac cone surface states in the Bi_2Se_3 material class.

As a matter of fact, a nonzero (nontrivial) topological mirror number does not require a nonzero Z_2 topological number. Or in other word, there is no necessary correlation between a mirror symmetry protected topological order and a time-reversal symmetry protected topological order. However, since most of the Z_2 topological insulators ($Bi_{1-x}Sb_x$, Bi_2Se_3, Bi_2Te_3 and etc.) also possess mirror symmetries in their crystalline form, thus topological mirror order n_M typically coexists with the strong Z_2 topological order, and only manifests itself as the chirality or the handness of the spin texture. One possible way to isolate the mirror topological order from the Z_2 order is to work with systems that feature an even number of bulk band inversions. This approach naturally exclude a nontrivial Z_2 order which strictly requires an odd number of band inversions. More importantly, if the locations of the band inversions coincide with the mirror planes in momentum space, it will lead to a topologically nontrivial phase protected by the mirror symmetries of the crystalline system that is irrelevant to the time-reversal sym-

metry protection and the Z_2 (Kane-Mele) topological order. Such exotic new phase of topological order, noted as topological crystalline insulator [101] protected by space group mirror symmetries, has very recently been theoretically predicted and experimentally identified in the $Pb_{1-x}Sn_xTe(Se)$ alloy systems [36–38, 102]. An anomalous $n_M = -2$ topological mirror number in $Pb_{1-x}Sn_xTe$, distinct from the $n_M = -1$ case observed in the Z_2 topological insulators, has also been experimentally determined using spin-resolved ARPES measurements as shown in Ref. [37]. Moreover, the mirror symmetry can be generalized to other space group symmetries, leading to a large number of distinct topological crystalline insulators awaited to be discovered, some of which are predicted to exhibit nontrivial crystalline order even without spin-orbit coupling as well as topological crystalline surface states in non-Dirac (e.g. quadratic) fermion forms [101].

In 3D Z_2 (Kane-Mele) TIs, the spin-resolved experimental measurements shown above reveal an intimate and straightforward connection between the topological numbers (ν_0, n_M) and the nontrivial Berry's phase. The ν_0 determines whether the surface electrons support a non-trivial Berry's phase. The 2D Berry's phase is a critical signature of topological order and is not realizable in isolated 2D electron systems, nor on the surfaces of conventional spin-orbit or exchange coupled magnetic materials. A non-zero Berry's phase is known, theoretically, to protect an electron system against the almost universal weak-localization behavior in their low temperature transport [19, 103] and is expected to form the key element for fault-tolerant computation schemes [103, 104], because the Berry's phase is a geometrical agent or mechanism for protection against quantum decoherence [105]. Its remarkable realization on the $Bi_{1-x}Sb_x$ surface represents an unprecedented example of a 2D π Berry's phase, and opens the possibility for building realistic prototype systems to test quantum computing modules. In general, our results demonstrate that spin-ARPES is a powerful probe of 3D topological order, which opens up a new search front for topological materials for novel spin-devices and fault-tolerant quantum computing.

TOPOLOGICAL PROTECTION AND TUNABILITY OF THE SURFACE STATES OF A 3D TOPOLOGICAL INSULATOR

The predicted topological protection of the surface states of Sb implies that their metallicity cannot be destroyed by weak time reversal symmetric perturbations. In order to test the robustness of the measured gapless surface states of Sb, we introduce such a perturbation by randomly substituting Bi into the Sb crystal matrix. Another motivation for performing such an experiment is that the formalism developed by Fu and Kane [19] to calculate the Z_2 topological invariants relies on inversion symmetry being present in the bulk crystal, which they assumed to hold true even in the random alloy $Bi_{1-x}Sb_x$. However, this formalism is simply a device for simplifying the calculation and the non-trivial $\nu_0 = 1$ topological class of $Bi_{1-x}Sb_x$ is predicted to hold true even in the absence of inversion symmetry in the bulk crystal [19]. Therefore introducing light Bi substitutional disorder into the Sb matrix is also a method to examine the effects of alloying disorder and possible breakdown of bulk inversion symmetry on the surface states of Sb(111). We have performed spin-integrated ARPES measurements on single crystals of the random alloy $Sb_{0.9}Bi_{0.1}$. Figure 13 shows that both the surface band dispersion along $\bar{\Gamma}$-$\bar{M}$ as well as the surface state Fermi surface retain the same form as that observed in Sb(111), and therefore the 'topological metal' surface state of Sb(111) fully survives the alloy disorder. Since Bi alloying is seen to only affect the band structure of Sb weakly, it is reasonable to assume that the topological order is preserved between Sb and $Bi_{0.91}Sb_{0.09}$ as we observed.

In a simpler fashion compared to $Bi_{1-x}Sb_x$, the topological insulator behavior in Bi_2Se_3 is associated with a single band inversion at the surface Brillouin zone center. Owing to its larger bandgap compared with $Bi_{1-x}Sb_x$, ARPES has shown that its topological properties are preserved at room temperature [25]. Two defining properties of topological insulators, spin-momentum locking of surface states and π Berry phase, can be clearly demonstrated in the Bi_2Se_3 series. The surface states are protected by time-reversal symmetry symmetry, which implies that the surface Dirac node should be robust in the presence of nonmagnetic disorder. On the other hand, a gap at the Dirac point is theoretically expected to open in the presence of magnetism along the out-of-plane direction perpendicular to the sample surface. Here magnetism is required to break time-reversal symmetry whereas its out-of-plane direction is critical to break additional protections by crystalline-symmetries [101]. Unlike in theory, magnetism in real topological insulator materials exhibits complex phenomenology [32, 40, 106–111]. Experimental studies of a magnetic gap especially on the quantitative level is challenging because many other physical or chemical changes are found to also lead to extrinsic gap-like feature at the Dirac point [44, 52, 110, 111]. We utilize spin-resolved angle-resolved photoemission spectroscopy to measure the momentum space spin configurations in systematically magnetically (Mn) doped, non-magnetically (Zn) doped, and ultra-thin quantum coherent topological insulator films [35]. Fig. 14b shows the out-of-plane spin polarization (P_z) measurements of the electronic states in the vicinity of the Dirac point gap of a Mn(2.5%)-Bi_2Se_3 sample. The surface electrons at the time-reversal invariant $\bar{\Gamma}$ point (red curve in Fig. 14b) are clearly observed to be spin polarized in the out-of-plane direction. The opposite sign of P_z for the upper and lower Dirac band shows that the Dirac point spin degeneracy is indeed lifted up ($E(k_{//} = 0,\uparrow) \neq E(k_{//} = 0,\downarrow)$), which manifestly breaks the time-reversal symmetry on the surface of

our Mn(2.5%)-Bi_2Se_3 samples. Systematic spin-resolved measurements as a function of binding energy and momentum reveal a Hedgehog-like spin texture (inset of Fig. 14b). Such exotic spin groundstate in a magnetic topological insulator enables a tunable Berry's phase on the magnetized topological surface [35], as experimentally demonstrated by our chemical gating via NO_2 surface adsorption method shown in Figs. 14c and d.

Many of the interesting theoretical proposals that utilize topological insulator surfaces require the chemical potential to lie at or near the surface Dirac point. This is similar to the case in graphene, where the chemistry of carbon atoms naturally locates the Fermi level at the Dirac point. This makes its density of carriers highly tunable by an applied electrical field and enables applications of graphene to both basic science and microelectronics. The surface Fermi level of a topological insulator depends on the detailed electrostatics of the surface and is not necessarily at the Dirac point. Moreover, for naturally grown Bi_2Se_3 the bulk Fermi energy is not even in the gap. The observed n-type behavior is believed to be caused Se vacancies. By appropriate chemical modifications, however, the Fermi energy of both the bulk and the surface can be controlled. This allowed [25] to reach the sweet spot in which the surface Fermi energy is tuned to the Dirac point (Fig.15). This was achieved by doping bulk with a small concentration of Ca, which compensates the Se vacancies, to place the Fermi level within the bulk band gap. The surface was the hole doped by exposing the surface to NO_2 gas to place the Fermi level at the Dirac point, and has been shown to be effective even at room temperature (Fig.16). These results collectively show how ARPES can be used to study the topological protection and tunability properties of the 2D surface of a 3D topological insulator.

These techniques to identify, characterize and manipulate the topological bulk and surface states of 3D topological insulators have opened the way for performing surface sensitive transport measurements on bulk crystals [54, 55], exfoliated nano-devices [57, 58] and thin films [60–62] as well as surface sensitive optical measurements [67, 73].

FUTURE DIRECTIONS: TOPOLOGICAL SUPERCONDUCTORS AND TOPOLOGICAL CRYSTALLINE INSULATORS

Recent measurements [28] show that surface instabilities cause the spin-helical topological insulator band structure of Bi_2Se_3 to remain well defined and non- degenerate with bulk electronic states at the Fermi level of optimally doped superconducting $Cu_{0.12}Bi_2Se_3$, and that this is also likely to be the case for superconducting variants of p-type Bi_2Te_3. These surface states provide a highly unusual physical setting in which superconductivity cannot take a conventional form, and is expected to realize one of two novel states that have not been identified elsewhere in nature. If superconducting pairing has even parity, as is nearly universal among the known superconducting materials, the surface electrons will achieve a 2D non-Abelian superconductor state with non-commutative Majorana fermion vortices that can potentially be manipulated to store quantum information. Surface vortices will be found at the end of bulk vortex lines as drawn in Fig.17. If superconducting pairing is odd, the resulting state is a novel state of matter known as a "topological superconductor" with Bogoliubov surface quasi-particles present below the superconducting critical temperature of 3.8 K. As drawn in Fig.17(c), these low temperature surface states would be gapless, likely making it impossible to adiabatically manipulate surface vortices for quantum computation. The unique physics and applications of the topological superconductor state are distinct from any known material system, and will be an exciting vista for theoretical and experimental exploration if they are achieved for the first time in $Cu_xBi_2Se_3$.

Another interesting frontier involves a newly discovered topological phase of matter, namely a topological crystalline insulator where space group symmetries replace the role of time-reversal symmetry in a Z_2 topological insulator [36–38, 101, 102, 115]. In Ref. [37], we experimentally investigate the possibility of a mirror symmetry protected topological phase transition in the $Pb_{1-x}Sn_xTe$ alloy system, which has long been known to contain an even number of band inversions based on band theory. We show that at a composition below the theoretically predicted band inversion, the system is fully gapped [37], whereas in the inverted regime, the surface exhibits even number of spin-polarized Dirac cone states revealing mirror-protected topological order distinct from that observed in $Bi_{1-x}Sb_x$ and Bi_2Se_3. Fig. 18 presents a comparison between the $Pb_{0.6}Sn_{0.4}Te$ and a single Dirac cone Z_2 topological insulator (TI) $GeBi_2Te_4$ [29]. In clear contrast to $GeBi_2Te_4$, which features a single spin helical Dirac cone enclosing the time-reversal invariant (Kramers') $\bar{\Gamma}$ point [Fig. 18(a-d)], none of the surface states of $Pb_{0.6}Sn_{0.4}Te$ is observed to enclose any of the time-reversal invariant momentum, demonstrating their irrelevance to the time-reversal symmetry related protection. On the other hand, all of the $Pb_{0.6}Sn_{0.4}Te$ surface states are found to locate along the two independent momentum space mirror line ($\bar{\Gamma}-\bar{X}-\bar{\Gamma}$) directions, revealing their topological protection as a consequence of the crystalline mirror symmetries of the $Pb_{1-x}Sn_xTe$ system [37]. The irrelevance to time-reversal symmetry observed in Ref. [37] suggests the potential to realize magnetic yet topologically protected surface states on the $Pb_{1-x}Sn_xTe$ surface, which is fundamentally not possible in the Z_2 topological insulator systems. In general, our discovery of a mirror symmetry protected topological phase in the $Pb_{1-x}Sn_xTe$ system opens the door for a wide range of exotic new physics, such as Lifshitz transition and Fermi surface Fractionalization based on topological surface states [102], topological antiferromagnetic insu-

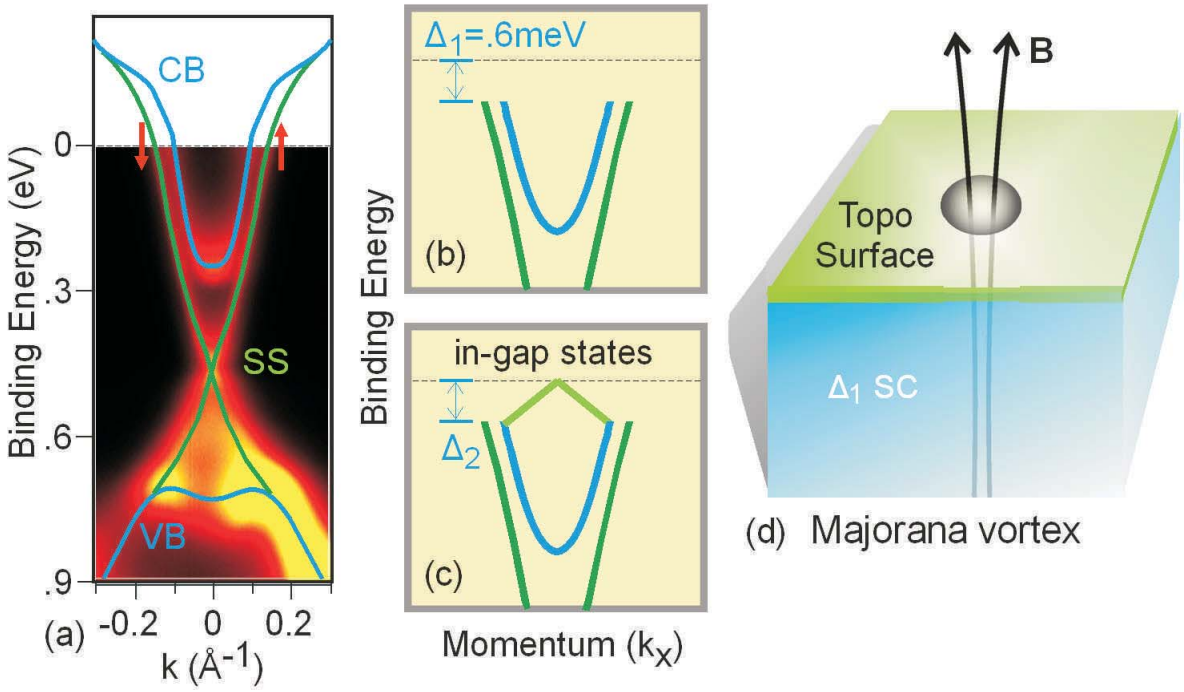


FIG. 17. **A Majorana platform.** (a) Topologically protected surface states cross the Fermi level before merging with the bulk valence and conduction bands in a lightly doped topological insulator. (b) If the superconducting wavefunction has even parity, the surface states will be gapped by the proximity effect, and vortices on the crystal surface will host braidable Majorana fermions. (c) If superconducting parity is odd, the material will be a so-called topological superconductor, and new states will appear below T_c to span the bulk superconducting gap. (d) Majorana fermion surface vortices are found at the end of bulk vortex lines and could be manipulated for quantum computation if superconducting pairing is even. [Adapted from L. Wray *et al.*, *Nature Phys.* **6**, 855 (2010). [28]]

lator [112, 113] and topological crystalline superconductor [114, 116] via bulk doping or proximity interfacing, as well as new topological crystalline orders protected by other point group symmetries even without spin-orbit interactions [101].

Acknowledgement The authors acknowledge A. Bansil, H. Lin, C. L. Kane, A. V. Fedorov, J.H. Dil, J. Osterwalder and D. Qian for collaboration; R.J. Cava, N. Samarth and F.C. Chou groups for samples; and U.S. DOE/BES DE-FG-02-05ER46200 for primary support. Authors also acknowledge invaluable technical support from many scientists at national and international facilities including Advanced Light Source (LBNL), Stanford Synchrotron facility (SSRL/SLAC), Swiss Light Source (SLS), Wisconsin Synchrotron facility (SRC) and MaxLab (Lund/Sweden). M.Z.H. acknowledges partial support for sample growth through ACI Fellowship and visiting scientist support from Lawrence Berkeley National Laboratory and additional support from A.P. Sloan Foundation and Princeton University.

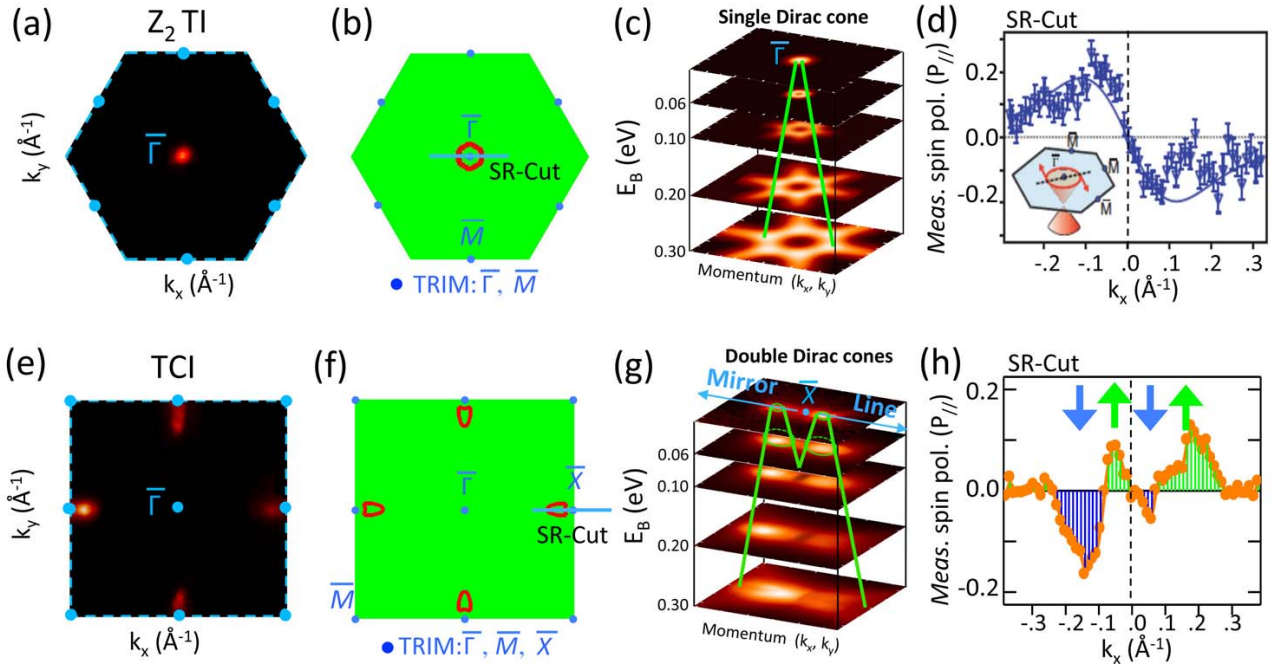


FIG. 18. **The topological distinction between Z_2 (Kane-Mele) topological insulator and topological crystalline insulator phases.** (a-d) ARPES, spin-resolved ARPES and calculation results of the surface states of a Z_2 topological insulator $GeBi_2Te_4$ [29], an analog to Bi_2Se_3 [23]. (a) ARPES measured Fermi surface with the chemical potential tuned near the surface Dirac point. (b) First-principles calculated iso-energetic contour of the surface states near the Dirac point. The solid blue line shows the momentum-space cut used for spin-resolved measurements. Right: A stack of ARPES iso-energetic contours near the $\bar{\Gamma}$ point of the surface BZ. (d) Measured spin polarization of Bi_2Se_3, in which a helical spin texture is revealed. (e-h) ARPES and spin-resolved ARPES measurements on the $Pb_{0.6}Sn_{0.4}Te$ ($x = 0.4$) samples and band calculation results on the end compound SnTe [102]. (e) ARPES measured Fermi surface map of $Pb_{0.6}Sn_{0.4}Te$. (f) First-principles calculated iso-energetic contour of SnTe surface states near the Dirac point. The solid blue line shows the momentum-space cut near the surface BZ edge center $\bar{X}$ point, which is used for spin-resolved measurements shown in panel (h). (g) A stack of ARPES iso-energetic contours near the $\bar{X}$ point of the surface BZ, revealing the double Dirac cone contours near each $\bar{X}$ point on the surface of $Pb_{0.6}Sn_{0.4}Te$. (h) Measured spin polarization of $Pb_{0.6}Sn_{0.4}Te$ near the native Fermi energy along the momentum space cut defined in panel (f), in which two spin helical Dirac cones are observed near an $\bar{X}$ point. [Adapted from S.-Y. Xu *et al.*, *Nature Comm.* **3**, 1192 (2012). [37]. Without spin measurements it is not possible to identify TCI surface states hence no proof of the TCI phase was possible prior to the measurements in Ref-[37].]

[1] M. Z. Hasan & C. L. Kane, *Rev. Mod. Phys.* **82**, 3045-3067 (2010).
[2] J. E. Moore, *Nature* **464**, 194-198 (2010).
[3] M. Z. Hasan & J. E. Moore, *Ann. Rev. Cond. Mat. Phys.* **2**, 55-78 (2011).
[4] X.-L. Qi & S.-C. Zhang, *Rev. Mod. Phys.* **83**, 1057 (2011).
[5] L. Fu, C. L. Kane & E. J. Mele, *Phys. Rev. Lett.* **98**, 106803 (2007).
[6] R. Roy, *Phys. Rev. B* **79**, 195322 (2009).
[7] J. E. Moore & L. Balents, *Phys. Rev. B* **75**, 121306(R) (2007).
[8] D. Hsieh, *et al.*, *Nature* **452**, 970 (2008) [Completed and submitted in **2007**]. Also see KITP Proceeding at http://online.itp.ucsb.edu/online/motterials07/hasan/ **(2007)**.
[9] N. W. Ashcroft & N. D. Mermin, *Solid State Physics* (Holt, Rinehart and Winston, New York, 1976).
[10] K. v. Klitzing, G. Dorda & M. Pepper, *Phys. Rev. Lett.* **45**, 494 (1980).
[11] D. C. Tsui, H. L. Stormer, & A. C. Gossard, *Phys. Rev. Lett.* **48**, 1559 (1982).
[12] R. B. Laughlin, *Phys. Rev. Lett.* **50**, 1395 (1983).
[13] X.-G. Wen, *Int. J. Mod. Phys. B* **4**, 239 (1990).
[14] D. J. Thouless, *et al.*, *Phys. Rev. Lett.* **49**, 405 (1982).
[15] J. E. Avron, D. Osadchy & R. Seiler, *Phys. Today* **56** (8), 38 (2003).
[16] C. L. Kane & E. J. Mele, *Phys. Rev. Lett.* **95**, 146802 (2005).
[17] B. A. Bernevig, T. L. Hughes & S.-C. Zhang, *Science* **314**, 1757 (2006).
[18] M. König, *et al.*, *Science* **318**, 766 (2007).
[19] L. Fu & C. L. Kane, *Phys. Rev. B* **76**, 045302 (2007).
[20] L. Fu, C. L. Kane & E. J. Mele, *Phys. Rev. Lett.* **98**, 106803 (2007).
[21] D. Hsieh, *et al.*, *Nature* **452**, 970 (2008).
[22] D. Hsieh, *et al.*, *Science* **323**, 919 (2009).
[23] Y. Xia, *et al.*, *Nature Phys.* **5**, 398 (2009).
[24] H. Zhang, *et al.*, *Nature Phys.* **5**, 438 (2009).
[25] D. Hsieh, *et al.*, *Nature* **460**, 1101 (2009).
[26] Y. L. Chen *et al.*, *Science* **325**, 178 (2009).
[27] D. Hsieh, *et al.*, *Phys. Rev. Lett.* **103**, 146401 (2009).
[28] L. A. Wray, *et al.*, *Nature Phys.* **6**, 855 (2010).
[29] Su-Yang Xu, *et al.*, Preprint at http://arXiv.org/abs/1007.5111 (2010).
[30] H. Lin, *et al.*, *Nature Mat.* **9**, 546 (2011).
[31] H. Lin, *et al.*, *Phys. Rev. Lett.* **105**, 036404 (2011).
[32] L. A. Wray, *et al.*, *Nature Phys.* **7**, 32 (2011).
[33] Su-Yang Xu, *et al.*, *Science* **332** 560 (2011).
[34] M. Neupane, *et al.*, *Phys. Rev. B* **85**, 235406 (2012).
[35] Su-Yang Xu, *et al.*, *Nature Phys.* **8**, 616 (2012).
[36] P. Dziawa, *et al.*, *Nature Mat.* **11**, 1023 (2012).
[37] Su-Yang Xu, *et al.*, *Nature Commun.* **3**, 1192 (2012).
[38] Y. Tanaka, *et al.*, *Nature Phys.* **8**, 800 (2012).
[39] Y. Zhang, *et al.*, *Nature Phys.* **6**, 584 (2010).
[40] Y.-L. Chen, *et al.*, *Science* **329**, 659 (2010).
[41] T. Sato, *et al.*, *Phys. Rev. Lett.* **105**, 136802 (2010).
[42] K. Kuroda, *et al.*, *Phys. Rev. Lett.* **105**, 146801 (2010).
[43] P.D.C. King, *et al.*, *Phys. Rev. Lett.* **107**, 096802 (2011).
[44] T. Sato, *et al.*, *Nature Phys.* **7**, 840 (2011).
[45] Z. Pan, *et al.*, *Phys. Rev. Lett.* **108**, 117601 (2012).
[46] P. Roushan, *et al.*,*Nature* **460**, 1106 (2009).
[47] T. Zhang, *et al.*,*Phys. Rev. Lett.* **103**, 266803 (2009)
[48] Z. Alpichshev, *et al.*,*Phys. Rev. Lett.* **104**, 016401 (2010).
[49] P. Cheng, *et al.*, *Phys. Rev. Lett.* **105**, 076801 (2010).
[50] T. Hanaguri, *et al.*, *Phys. Rev. B* **82**, 081305 (2010).
[51] J. Seo, *et al.*, *Nature* **466**, 343 (2010).
[52] H. Beidenkopf, *et al.*, *Nature Phys.* **7**, 939 (2011).
[53] Y. Okada, *et al.*, *Phys. Rev. Lett.* **106**, 206805 (2011).
[54] D.-X. Qu, *et al.*, *Science* **329**, 821 (2010).
[55] J. G. Analytis, *et al.*, *Nature Phys.* **6**, 960 (2010).
[56] H. L. Peng, *et al.*, *Nature Mat.* **9**, 225 (2010).
[57] H. Steinberg *et al.*, *Nano Lett.* **10**, 5032 (2010).
[58] J. Chen, *et al.*, *Phys. Rev. Lett.* **105**, 176602 (2010).
[59] Z. Ren, *et al.*, *Phys. Rev. B* **82**, 241306 (2011).
[60] H. T. He, *et al.*, *Phys. Rev. Lett.* **106**, 166805 (2011).
[61] M. Liu, *et al.*, *Phys. Rev. B* **83**, 165440 (2011).
[62] J. Wang, *et al.*, *Physical Review B* **83**, 245538 (2011).
[63] B. Sacépé, *et al.*, *Nature Comm.* **2**, 575 (2011).
[64] D. Kim, *et al.*, *Nature Phys.* **8**, 459 (2012).
[65] J. G. Checkelsky, *et al.*, *Nature Phys.* **8**, 729 (2012).
[66] Y. H. Wang, *et al.*, *Phys. Rev. Lett.* **107**, 207602 (2011).
[67] D. Hsieh, *et al.*, *Phys. Rev. Lett.* **106**, 057401 (2011).
[68] S. R. Park, *et al.*, *Phys. Rev. Lett.* **108**, 046805 (2012).
[69] J. A. Sobota, *et al.*, *Phys. Rev. Lett.* **108**, 117403 (2012).
[70] Y. H. Wang, *et al.*, *Phys. Rev. Lett.* **109**, 127401 (2012).
[71] A. A. Schafgans, *et al.*, *Phys. Rev. B* **85**, 195440 (2012).
[72] J. W. McIver, *et al.*, *Nature Nanotechnology* **7**, 96 (2012).
[73] R. Valdés Aguilar, *et al.*, *Phys. Rev. Lett.* **108**, 087403 (2012).
[74] S. Murakami, *New. J. Phys.* **9**, 356 (2007).
[75] B. Lenoir, *et al.*, Bi-Sb alloys: an update. *Fifteenth International Conference on Thermoelectrics*, 1-13 (1996).
[76] Y. Liu & E. Allen, *Phys. Rev. B* **52**, 1566 (1995).
[77] P. A. Wolff, *J. Phys. Chem. Solids* **25**, 1057 (1964).
[78] H. Fukuyama & R. Kubo, *J. Phys. Soc. Jpn.* **28**, 570 (1970).
[79] F. A. Buot, *Phys. Rev. A* **8**, 1570 (1973).
[80] L. C. Hebel & G. E. Smith, *Phys. Lett.* **10**, 273 (1964).
[81] Y. Zhang, *et al.*, *Nature* **438**, 201 (2005).
[82] S. Zhou, *et al.*, *Nature Mat.* **6**, 770 (2007).
[83] F. D. M. Haldane, *Phys. Rev. Lett.* **61**, 2015 (1988).
[84] C. R. Ast & H. Hochst, *Phys. Rev. Lett.* **87**, 177602 (2001).
[85] H. Hochst & S. Gorovikov, *J. Elect. Spectrosc. Relat. Phenom.* **351**, 144 (2005). This work does not measure along the critical $\bar{\Gamma} - \bar{M}$ direction or detect the bulk Dirac spectrum near L.
[86] P. Hofmann, *Prog. Surf. Sci.* **81**, 191 (2006).
[87] T. Hirahara, *et al.*, *Phys. Rev. B* **76**, 153305 (2007).
[88] M. Hengsberger, *et al.*, *Eur. Phys. J.* **17**, 603 (2000).
[89] C. R. Ast & H. Hochst, *Phys. Rev. B* **67**, 113102 (2003).
[90] K. S. Novoselov, *et al.*, *Science* **315**, 1379 (2007).
[91] J. C. Y. Teo, L. Fu & C. L. Kane, *Phys. Rev. B* **78**, 045426 (2008).
[92] J. J. Sakurai, *Modern Quantum Mechanics* (Addison-Wesley, New York, 1994).
[93] S. Hufner, *Photoelectron Spectroscopy* (Springer-. verlag, Berlin, 1995).
[94] T. Hirahara, *et al.*, *Phys. Rev. B* **76**, 153305 (2007).

[95] M. Hoesch, *et al.*, *Phys. Rev. B* **69**, 241401(R) (2004).
[96] K. Sugawara, *et al.*, *Phys. Rev. Lett.* **96**, 046411 (2006).
[97] X. -L. Qi, T. Hughes & S. -C. Zhang, *Phys. Rev. B* **78**, 195424 (2008).
[98] M. Hoesch, *et al.*, *J. Electron Spectrosc. Relat. Phenom.* **124**, 263 (2002).
[99] T. J. Gay & F. B. Dunning, *Rev. Sci. Instrum.* **63**, 1635 (1992).
[100] F. Meier, *et al.*, *Phys. Rev. B* **77**, 165431 (2008).
[101] L. Fu, *Phys. Rev. Lett.* **106**, 106802 (2011).
[102] H. Hsieh, *et al.*, *Nature Commun.* **3**, 982 (2012).
[103] L. Fu & C. L. Kane, *Phys. Rev. Lett.* **100**, 096407 (2008).
[104] P. J. Leek, *et al.*, *Science* **318**, 1889 (2007).
[105] A. Kitaev, *Ann. Phys. (NY)* **303**, 2 (2003).
[106] Y. S. Hor, *et al.*, *Phys. Rev. B* **81**, 195203 (2010).
[107] H.W. Ji, *et al.*, *Phys. Rev. B* **85**, 165313 (2012)
[108] Z. Salman, *et al.*, Preprint at http://arXiv:1203.4850 (2012).
[109] I. Vobornik, *et al.*, *Nano Lett.* **11**, 4079 (2011).
[110] S.V. Eremeev, *et al.*, Preprint at http://arXiv:1107.3208 (2011).
[111] Su-Yang Xu, *et al.*, Preprint at http://arXiv.org/abs/1206.0278 (2012).
[112] T. Story, *et al.*, *Phys. Rev. Lett.* **56**, 777 (1986).
[113] R. S. K. Mong, *et al.*, *Phys. Rev. B* **81**, 245209 (2010).
[114] S. Sasaki, *et al.*, *Phys. Rev. Lett.* **109**, 217004 (2012)
[115] Y. Ando *J. Phys. Soc. Jpn.* **82**, 102001 (2013)
[116] J. C. Y. Teo & T. L. Hughes, *Phys. Rev. Lett.* **111**, 047006 (2013)